PENETRATIVE DEFORMATION OF DOLOSTONES DURING CONTACT METAMORPHISM AND THE FORCEFUL EMPLACEMENT OF THE TUNGSTONIA GRANITE, KERN MOUNTAINS, NEVADA

A Thesis

by

KYLE PATRICK GOODSON

Submitted to the Office of Graduate and Professional Studies of
Texas A&M University
in partial fulfillment of the requirements for the degree of

MASTER OF SCIENCE

Chair of Committee,	Andreas Kronenberg
Committee Members,	Will Lamb
	Julie Newman
	David Sparks
	Ibrahim Karaman
Head of Department,	Rick Giardino

August 2014

Major Subject: Geology

ABSTRACT

Foliated dolostones surrounding the Tungstonia granite of eastern Nevada were investigated with the purpose of testing for models of forceful emplacement. Intragranular strains and lattice-preferred orientations (LPOs) define a zone of penetrative deformation that is narrow (<400 m) relative to the size of the Tungstonia granite (radius ~5 km) and coincident with its metamorphic contact aureole. Principle intragranular strains show shortening perpendicular to the granite-dolostone contact with maximum elongations that vary with position but are commonly parallel to the contact-parallel lineation. States of strain range from nearly pure flattening to plane strain. LPOs within ~50 m of the granite-dolostone contact exhibit c-axis maxima that are inclined to the foliation normal, indicating a sense of shear consistent with the ascent of the granite body relative to the surrounding carbonates. Penetrative deformation of dolostones is restricted to the contact metamorphic aureole with temperatures of ~300 to 710°C given by calc-silicate phase relations, calcite-dolomite geothermometry, and granite melting relations. Metamorphic constraints on peak temperatures and simple heat flow modeling suggest surprisingly short times of ~100 to 2,200 years for conductive heat exchange and pluton emplacement. Combined with constraints of temperature, pressure, strain, and grain size, strain rates near the granite-dolostone contact compare favorably with strain rates predicted by flow laws for dolomite evaluated at high strain rates in experimental studies. Penetrative deformation of dolostones closest to the granite-carbonate contact may involve a mixture of both dislocation and diffusion creep, while deformation further from the contact appears to be dominated by intracrystalline dislocation creep.

ACKNOWLEDGEMENTS

I would like to thank my committee chair, Dr. Andreas Kronenberg, and my committee members, Dr. Will Lamb, Dr. Julie Newman, Dr. David Sparks, and Dr. Ibrahim Karaman, for their guidance and support throughout the course of this study. In particular, I would especially like to express my gratitude to my advisor, Dr. Andreas Kronenberg, for taking me on after extenuating circumstances and offering himself as a mentor to me. This project would not have been possible without the work of Bill Shea. His contributions are greatly appreciated and I hope he will be proud of the results his efforts have lead to. I would also like to thank Dr. Caleb Holyoke III, Dr. Ray Guillemette, Rachel Wells, and Harold Johnson for their extensive assistance in several facets of this study and guidance throughout my graduate school experience. Additional thanks goes to Patrick Wagner for his assistance in grain tracing. Support for my tuition was provided by scholarships from the Houston Geological Society and Texas A&M Association of Former Students. The FE-SEM acquisition and Electron Microprobe work were supported by the National Science Foundation grant DBI-0116835.

I would like to take this opportunity to also thank Dr. David Wiltschko for accepting me as a graduate student and for offering himself as a mentor. My only regret is that we did not have more time to work together.

Lastly, thanks to my mother, father, sisters, brother, and Cristina Enders for their continued encouragement over the last several years.

NOMENCLATURE

BSE	Backscatter electrons
Cc	Calcite
CPO	Crystallographic-preferred orientation
Di	Diopside
Dol	Dolomite
EBSD	Electron backscatter diffraction
EDS	Energy dispersive spectroscopy
LPO	Lattice-preferred orientation
Mic	Microcline
Q	Quartz
SE	Secondary electrons
SEM	Scanning electron microscopy
T	Temperature
Tr	Tremolite
XMg	Magnesium composition

TABLE OF CONTENTS

LIST OF FIGURES

Page

LIST OF TABLES

I. INTRODUCTION

The subsurface transport and emplacement of magma requires deformations of surrounding country rocks. At low pressures and background temperatures of the upper crust, deformations may be accompanied by fractures, and magma may fill opening cracks to form dikes and sills (Pollard, 1976; Delaney & Pollard, 1981, 1986; Lister & Kerr, 1991; Clemens & Mawer, 1992; Petford et al., 1993). Given sufficient magma pressures, dikes and sill may be enlarged, and inflation, accommodated by flexure of overlying rocks, may form laccoliths of significant size (Gilbert, 1877; Pollard, 1973; Pollard & Muller, 1976; Pollard & Holzhausen, 1979; Paterson et al., 1991; Morgan et al., 1998; Saint-Blanquat et al., 2001; Gerbi et al., 2004). At greater depths of the middle to lower crust, however, greater lithostatic loads suppress brittle processes and magma pressures are not sufficient for displacement or flexure of overlying strata. At elevated temperatures and pressures, penetrative deformations of country rocks may accommodate magma ascent and emplacement by crystal plastic processes. However, the emplacement of volumetrically large granitic plutons appears to require significant strains and displacements of country rock (Holder, 1979; Marsh, 1982; Weinberg & Podladchikov, 1994; Miller & Paterson, 1999; Gerbi et al., 2004; Zak & Paterson, 2006). Thus, the mechanics and processes of intrusion of large-scale plutons remain controversial (Lister & Kerr, 1991; Clemens & Mawer, 1992; Petford, 1996; Clemens, 1998; Miller & Paterson, 1999). Competing forceful emplacement models attempting to solve the ‘room problem’ (replacing the country rock volume by an equivalent volume of magma) involve stoping, inflation (ballooning and upward displacement), diapiric flow of magma, and tectonic displacement (Grout, 1945; Holder, 1979; Marsh, 1982; Schmeling et al., 1988; Brown & Solar, 1999; Tikoff et al., 1999; Marko & Yoshinobu, 2011).

1.1 Mechanics of intrusion

Dike and sill formation (Figure 1a) have been modeled by fracture mechanics of fluid-filled cracks (Weertman, 1971; Pollard & Muller, 1976; Delaney & Pollard, 1981; Delaney et al., 1986; Lister & Kerr, 1991; Clemens & Mawer, 1992; Clemens, 1998). Thus, magma may infiltrate rocks along fractures and joints and thereby ascend to shallow depths with little penetrative deformation of surrounding rocks. In studying the intrusions and minette dikes near Ship Rock, New Mexico, Delaney and Pollard (1981) utilized mechanical models to analyze dike propagation, and proposed this as the dominant mechanism for passing a pressurized volume of magma through brittle/elastic host rocks. The thermal and pressure efficiency of dikes and sills as transport mechanisms of magma to shallow depths has been studied extensively (Gudmundsson, 1984; Lister & Kerr, 1991; Clemens & Mawer, 1992; Clemens, 1998; Gerbi et al., 2004) and have been linked as feeders for large-body laccoliths.

Gilbert (1977) first proposed the concept of a laccolith (Figure 1b) and the potential for metamorphic deformation of the surrounding country rock after observing the “mushroom-like” bulging and steep dips of strata in the Henry Mountains. He further postulated that sheet intrusions start as sheet sills, they occur due to relative

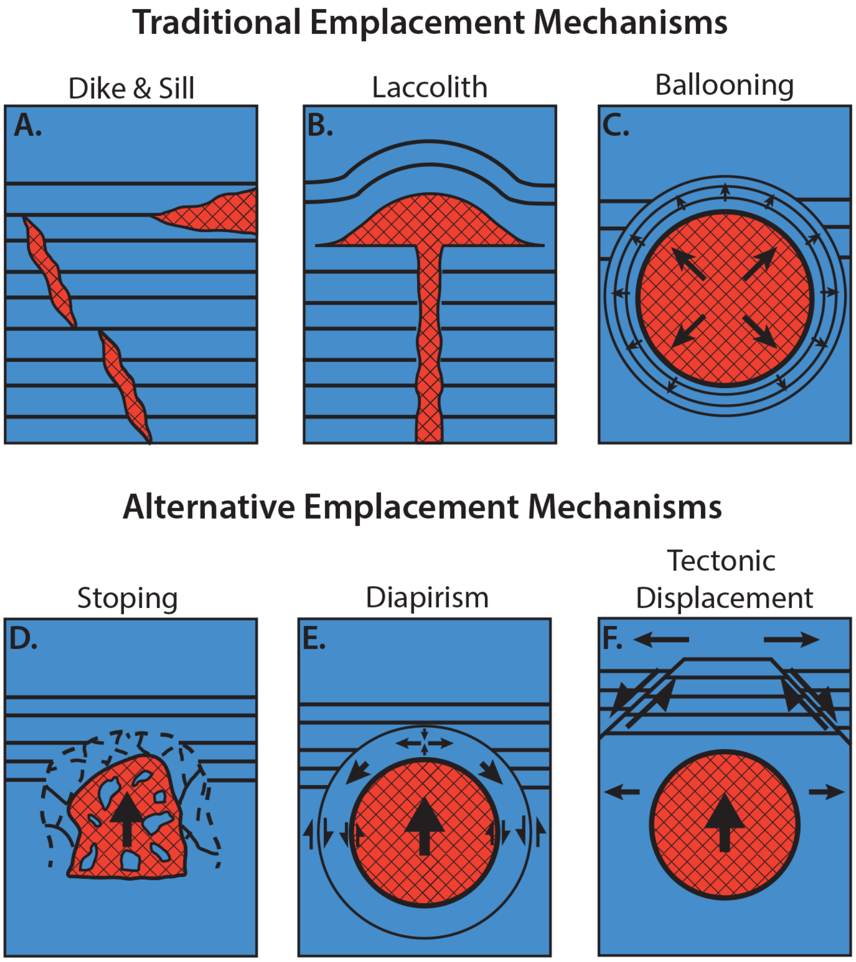

Figure 1. Models of magma ascent, intrusion, and emplacement. (a) Dikes and sills modeled as fluid-filled cracks in elastic brittle country rocks; (b) Laccolith model of larger magma intrusions due to the inflation of a sill and upwards displacement of country rocks; (c) Ballooning occurs when a fast-moving magma intrusion forms a large chamber emplacement and pushes outward forcing compaction and foliations to occur within the host rock (Modified from Gilbert, 1877; Marsh, 1982; Shea et al., 1988); (d) Stoping occurs when the heat and pressure from an ascending intrusion cause overburden rock to fracture, after which melt and/or volatiles penetrate the newly-formed conduits and force blocks of host rock to dislodge and fall into chamber melt depending on the relative densities of the host rock and melt (Daly, 1903); (e) Magmatic diapirism involves channel flow of overburden rock out and around the main intrusion body as it ascends. Likely caused by the repeated activation of magma intrusion, shear is thought to occur between the intrusion and in-situ country rock. (Marsh, 1982); (f) Accommodated magma ascent by lateral displacements and extensional tectonics.

differences in density, and that these large bodies were likely fed by deep-sourced stocks. This mechanism of forming large magma intrusions has been confirmed by Hunt et al. (1953) and Pollard and Johnson (1973). Another notable site for laccolith studies, the Papoose Flat pluton of eastern California, shared many similar characteristics with the Henry Mountains, including evidence of sheet intrusion and uplift of the overburden while the magma chamber swelled (Pollard & Johnson, 1973; Pollard 1973, 1976; Saint-Blanquat et al., 2001), but there are two major differences between them: the sheet intrusion was forcibly emplaced within inclined strata and there is evidence that diking from the Sierra Nevada batholith could have been the source of magma (Sylvester et al., 1978; Pollard, 1976). Further study confirms the dike-to-laccolith formation of the body and supports the assumption that the two mechanisms may be more related than previously believed (Gerbi et al., 2004).

Models of magma ascent for large magma bodies must solve the ‘room problem’: what happens to the country rock as a magma body of significant volume is intruded. Magma intrusion by way of dikes or sills involving only small displacements of country rocks as fractures dilate and magma enters. Inflation of sills to form laccoliths may then occur if the magma pressure is high enough to uplift the overburden host rock, which has been demonstrated at shallow crustal depths (Delaney & Pollard, 1981; Clemens, 1998). However, a solution to the ‘room problem’ by uplift of host rocks of equivalent volume to large intrusive plutonic bodies (>10 sq.km) that ascend to intermediate depths of the crust and is challenging, and magma pressures are not sufficiently large to uplift the country rock above the ascending body. Models of magma ascent and emplacement at crustal levels are based either on stoping, in which fractured country rock drops to the base of the magma body as magma ascends, or on penetrative deformations of the host rock and diapiric rise of the magma (Daly, 1903; Marsh, 1982). In addition, extensional tectonic displacements may facilitate the introduction of large volume magma chambers, solving the room problem by large lateral displacements of country rock (Paterson & Fowler, 1993; Tikoff et al., 1999).

The emplacement of larger stocks and batholiths has been modeled based on stoping (Figure 1d), magma diapirism (Figure 1e), and ballooning (Figure 1c) (Daly, 1903; Marsh, 1982; Weinberg & Podladchikov, 1995; Holder, 1979). Stoping, proposed by Daly (1903), occurs when the heat and pressure from an ascending intrusion cause overburden rocks to fracture, after which melt and/or volatiles penetrate the newly formed cracks. With pervasive fracture, blocks of host rock may dislodge and fall into chamber melt, and depending on the relative densities of the host rock and melt may sink as magma ascends (Daly, 1903). Stoping provides a simple solution to the 'room problem', with sinking block volumes that are equivalent to the ascending magma volume. Marsh (1982) tested Daly's stoping concept by placing limits on the volumes of overburden rock that can pass through an intruding magmatic body without contaminating it chemically or cooling the magma sufficiently to crystallize it and stall its ascent. Despite the natural examples of magmatic stoping that are apparent, Marsh (1982) found that stoping can only explain small amounts of magma ascent.

Alternatively, large magma may ascend by "hot-Stokes" diapiric flow in which the viscosity of rocks surrounding the ascending magma bodies is decreased by thermal weakening (Figure 2; Grout, 1945; Marsh, 1982). Diapiric emplacement requires simple a density contrast between the intruding magma and surrounding host rock, localized simple shear, and channel flow of the surrounding overburden rock downwards to accommodate ascent of the magma body (Figure 2; Marsh, 1982). Numerical diapir models emphasize the importance of non-linear viscosities of the country rock to localized channel flow and thermal softening of the host rock, both of which make ascent more efficient while minimizing loss of heat from the magma (Weinberg & Podladchikov, 1994; Miller & Paterson, 1999; Albertz & Johnson, 2006; Polyansky et al., 2009, Polyansky et al., 2010; 2011; Paterson et al., 2011). Metamorphic aureoles and foliations associated with high temperature deformations are commonly observed surrounding intrusions (Miller & Gans, 1989; Paterson et al., 1991; Paterson & Miller, 1998; Brown & Solar, 1999; Tikoff et al., 1999; Zak & Paterson, 2006; Delle Piane et al., 2008). A less strict version of Marsh's model, dubbed a "visco-elastic diapir" (Miller & Paterson, 1999), considers the combination of power-law deformation and thermal softening.

Inflation (ballooning) of magma bodies (Figure 1c) also introduces penetrative strains in country rocks surrounding the pluton, though strain approaching pure shear are predicted by magma expansion and, as in laccolith formation, requires uplift at the Earth's surface or lateral displacements in extensional tectonic regimes (Holder, 1979; Marsh, 1982; Tikoff et al., 1999). Numerical diapiric models may include some component of ballooning accompanying the diapiric flow, the extent to which this occurs can be judged by penetrative strains that are coaxial pure shear versus simple shear.

In some studies of host rocks surrounding plutons, penetrative strains are small and cannot for large volumes of magma emplaced (Tikoff et al., 1999). In these cases, it appears that faulting and lateral tectonic displacements of the crust may have accommodated the pluton emplacement.

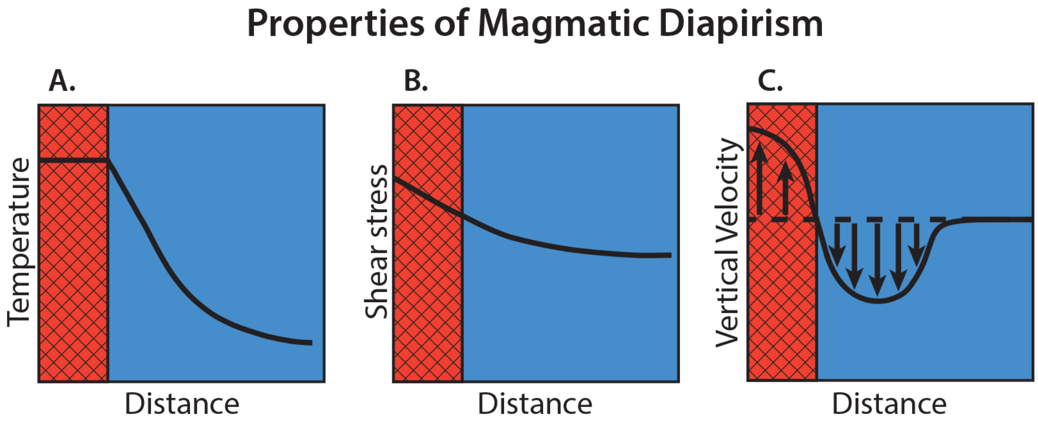

Figure 2. Properties of magmatic diapirism. Schematic profiles of temperature, shear stress, and vertical velocity of country rocks vs. distance from the intrusion, respectively. The red region represents intrusion and blue region represents the country rock. (a) Temperature declines dramatically with distance away from the intrusion due to thermal conduction; (b) Shear stress decreases with distance away from the intrusion, but changes in stress close to a large volume pluton are expected to be small; (c) Vertical velocity decreases, then increases slightly with distance from the intrusion (modified from Shea et al., 1988; Marsh, 1982).

1.2 Intrusion of the Tungstonia granite into dolostones of the Kern Mountains, Nevada

Deformed carbonates surrounding a granite stock in the Kern Mountains of eastern Nevada (Figure 3) offer the opportunity to investigate mechanisms of forceful emplacement of a large plutonic body at mid-crustal depths. Potential mechanisms of

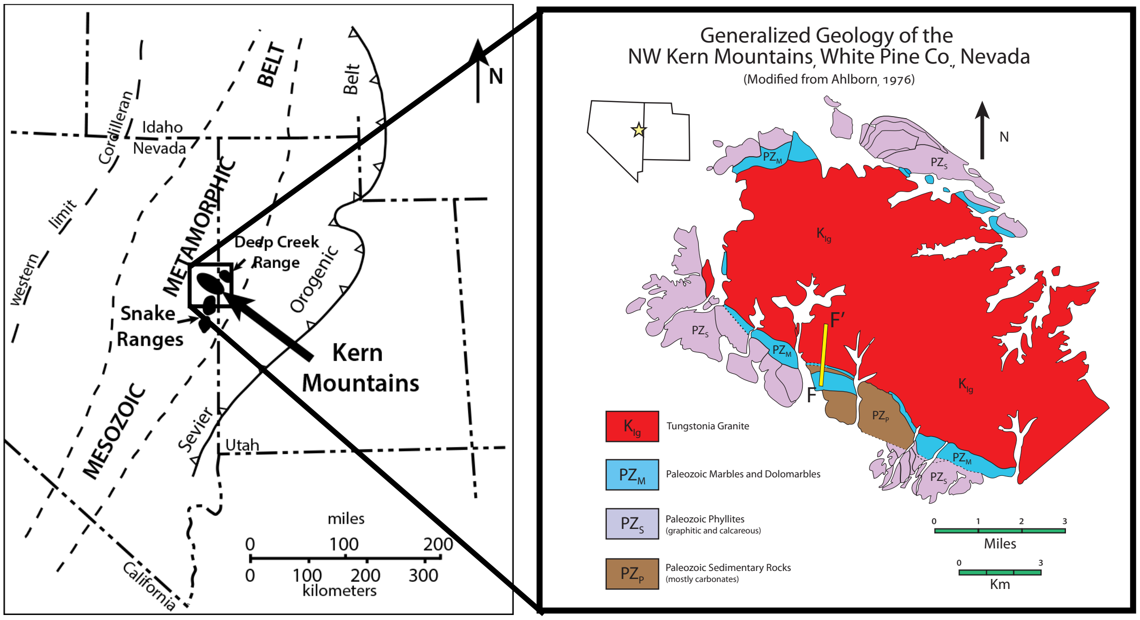

Figure 3. Location of the Kern Mountains and study traverse. The Tungstonia granite and surrounding Paleozoic carbonates exposed in the Kern Mountains of eastern Nevada and western Utah. In the left image, dashed lines indicate areas of Mesozoic metamorphism of Late Paleozoic sediments. Nearby ranges are the loci of several intrusions. The Deep Creek Range (north) and Snake Range (south), along with the Kern Mountains, make up a three-phase Late Mesozoic intrusion sequence (Best et al., 1974). The right image is a geologic outcrop map of the Tungstonia granite and surrounding carbonates of the Kern Mountains (modified from Best et al., 1974; Ahlborn, 1977).

intrusion are constrained by basic field relations and observations made of foliated dolostones surrounding the Tungstonia granite (with an approximate radius of ~5 km) and their relation to marginal foliations within the granite. The forceful emplacement of the magma body by diapir flow and/or ballooning assisted by thermal softening of surrounding carbonates is inferred from a number of field observations and constraints (Drewes, 1967; Best et al., 1974; Ahlborn, 1977; Shea et al., 1988):

- The contrasting compositions of the silicate melt and surrounding carbonates indicates that the granitic magma represents an intrusion and precludes anatexis or melting in place without magma transport.
- Dolostones surrounding the Tungstonia granite are foliated and some carbonates show lineations, with mesoscale foliations that appear strongest near the carbonate-granite contact and decrease in intensity with distance. Attitudes of carbonate foliations are sub-parallel to the carbonate-granite contact and wrap around the granite body in most geographic directions (Figure 4).
- Intensity of these carbonate foliations appears to scale with contact metamorphic conditions as judged by the occasional appearance of high temperature metamorphic minerals.
- Marginal granites of the Tungstonia are also foliated, with attitudes that are sub-parallel to the granite-carbonate contact and to the carbonate foliations (Figure 4). These foliations are interpreted to have formed at sub-solidus conditions once the granite had recrystallized at the pluton margins, and diapiric ascent and/or pluton expansion (ballooning) of the hyper-solidus center continued.
- Relatively homogeneous granite compositions throughout the characteristic two-mica Tungstonia granite (Armstrong, 1972; Sayeed, 1972; Sayeed et al., 1973; Best et al., 1974; Ahlborn, 1977) imply a single intrusion event rather than multiple smaller, episodic intrusion events. I focused my study on the intrusion of just this pluton but recognize that several other intrusion events occurred in the region that made up distinctly different granitic plutons (the Snake Range pluton and Deep

Creek Range pluton) (Nelson, 1959; Drewes, 1967; Armstrong, 1968; Lee & Christiansen, 1983; Barton & Trim, 1991).

- While nearby metamorphic rocks of the same lithology in this region (Nelson, 1959; Drewes, 1967; Lee & Christiansen, 1983; Gaudemer & Tapponier, 1987) have been deformed, associated with metamorphic core complexes of the Snake Range and Deep Creek Range pluton complexes, the Tungstonia granite and its marginal dolostones do not appear to have been affected by core-complex metamorphism and tectonics (Drewes. 1967; Best et al., 1974; Ahlborn, 1977; Shea et al., 1988; Barton & Trim, 1991). Thus, I was able to infer that deformation of dolostones surrounding the Tungstonia granite was related to its emplacement and contact metamorphism.
- Relatively few xenoliths within the Tungstonia granite, representing blocks of country rock incorporated into the magma body, have been observed (Drewes. 1967; Best et al., 1974; Shea et al., 1988). In addition, off-shooting dikes and fractures decorated by skarn mineralization in the country rocks are rare (Shea et al., 1988). In contrast to discordant contacts associated with fracture during magma intrusion and stoping (Marsh, 1982), the contact between Tungstonia granite and surrounding dolostones appears to be curvilinear. Taken together, these observations suggest that the contribution of stoping to magma ascent was probably very small.
- A number of small-scale normal faults are mapped in carbonates surrounding the Tungstonia granites that have strikes sub-parallel to the strike of the granite-carbonate contact. Displacements of country rock above these faults may have accommodated some of the magma emplacement; however, large-scale

displacements along faults, which could account for intrusion of the large volume of the Tungstonia granite body, are not apparent. Thus, accommodation of the Tungstonia granite during its emplacement by tectonic displacements can be ruled out.

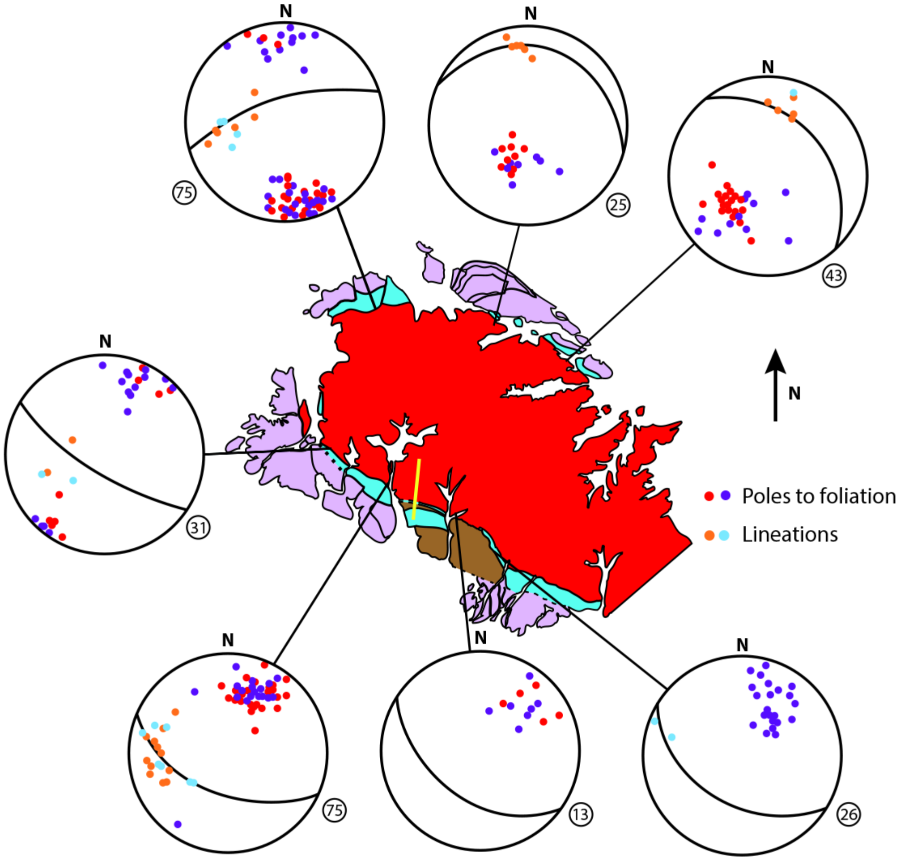

Figure 4. Poles to foliation and lineations in the Kern Mountain dolostones. The poles to foliation and lineations observed at the mesoscopic scale in dolostones across several sample traverses around the Tungstonia granite. The foliation around the intrusion clearly dips away from the center of pluton at varying angles. The circled numbers represent the number of measurements made for each area (data provided by W. Shea; modified from Ahlborn, 1977). The gold bar indicates the location of the “F” traverse.

In this study, I investigated dolostones surrounding the Tungstonia granite, characterizing their penetrative strains, lattice preferred orientations (LPO), and contact metamorphic conditions as a function of distance from the granite-carbonate contact. These results were compared with expected trends from a number of published intrusion models (Holder, 1979; Marsh, 1982; Schmeling et al., 1988; Weinberg & Podladchikov, 1994, 1995; Miller & Paterson, 1999; Tikoff et al., 1999; Polyanksky et al., 2009; Marko & Yoshinobu, 2011). In addition, these results may be compared with the deformation mechanisms and thermally activated flow laws for high temperature creep of dolomite (Davis et al., 2008; Delle Piane et al., 2008; Holyoke et al., 2013). Experimental studies of dislocation creep and diffusion creep of dolomite have evaluated values of activation energies, power law stress exponents, and grain size effects which I can compare with, bridging many orders in magnitude in strain rate, from the time scale of diapir intrusion to the experimental time scale.

II. BACKGROUND

This study benefited from previous modeling and observational studies of magma emplacement, geological studies of the Tungstonia granite and carbonates of the Kern Mountains, and analyses of experimental and naturally deformed dolomites.

2.1 Diapir and ballooning emplacement models

After observing the plastic behavior of several plutons of the Sierra Nevada, Marsh (1982) sought to further Grout's findings by analyzing three possible constraints: the viscosity (thermal sensitivity) of the wall rock (whereby drag is created), the size and shape of the ascending sphere, and, consequently, the resulting thermal cooling and crystallization of magma, which stalls further buoyant rise. The "hot-Stokes" diapir model of Marsh (1982) predicts ascent of an individual magma body of roughly half the value of the height of the intrusion through the overburden. For greater ascent distances, repeated pulses of magma are required over time for a late-stage magma to reach shallow depths (Marsh, 1982). Conduction of heat into the country rock and thermal softening of the host rock in the metamorphic aureole have since been modeled numerically (Schmeling, 1988; Weinberg & Podladchikov, 2004, 2005; Polyansky et al., 2009; Polyanksky et al., 2010; Paterson et al., 2011) and these processes appear to be to diapiric ascent. In characterizing the fabrics that occur around a diapir, pure shear flattening is expected at the top/roof of the magma body, a progression of strains along margins are expected to be plain strain, simple shear on the sides of the body, and elongation is expected below the diapir (Marsh, 1982; Schmeling et al., 1988; Zak & Paterson, 2006). By comparison with the channel flow predicted for Newtonian flow, non-linear viscous relations lead to narrow zones of penetrative deformation (Miller & Paterson, 1999; Albertz & Johnson, 2006). Despite these results, diapiric emplacement of large plutonic bodies and significant ascent distances in the crust remain controversial (Clemens et al., 1997)

Penetrative deformations of rocks surrounding intrusive plutons may also represent inflation (or ballooning) of the magma body when buoyancy forces are not sufficient for vertical diapiric flow (Reesor, 1958; Clifford, 1972; Holder, 1981). Several natural examples have been studied and support this mechanism (Reesor, 1958; Clifford, 1972; Holder, 1981). Unlike the strain patterns in country rocks surrounding a diapiric intrusion, strains surrounding an inflating pluton are expected to be coaxial with shortening perpendicular to the pluton's margins and extensional parallel to its margins.

The primary limitation on magma ballooning is the depth of emplacement and requirement for upward displacement of overburden. As long as an intrusion has magma pressures great enough to overcome overburden stresses, it is a viable mechanism for emplacement, especially at shallower depths where the overburden load is smaller and less magma pressure is required for uplift. However, the magma pressures required to forcefully displace country at great depths deeper than 10 km, for example, would have to be very high and potentially unrealistic. Studies critical of this process also point out that other mechanisms, like tectonic displacement and magmatic diapirism, may be necessary as the primary ascent mechanism with ballooning playing a minimal part during late stages of emplacement (Paterson & Vernon, 1995).

2.2 Metamorphic and deformation aureoles surrounding plutons

In addition to theoretical and numerical modeling studies of pluton emplacement, observational studies have constrained the mechanisms of intrusion. Miller and Paterson (1999) described 4 Cordilleran plutons (the Tenpeak pluton, Oval Peak pluton, Entiat pluton, and Hall Canyon pluton) emplaced at various depths within the crust, suggesting they exhibit separate stages of magmatic diapirism. The most consistent characteristics were the presence of contact-parallel foliations and lineations within the granite margins and metamorphic aureole in the country rocks and evidence of shear, observed at the field and microscopic scale, with a pluton-side-up and country rock-side-down sense of shear, as well as indicating downward channel flow of the host rock during emplacement (Miller & Paterson, 1999).

Forceful intrusion is not limited to plutons with metamorphic or deformation aureoles in surrounding host rocks. Translation (tectonic displacement) of overburden rock has been suggested as a primary mechanism of forceful emplacement, with natural examples to support this process. The study of several plutons in proximity to the Sierra Nevada batholith have produced models of extensional faulting that satisfy the ‘room problem’ by displacing overlying country rock laterally by up to 15 km (Hutton, 1988; Paterson & Fowler, 1993; Tikoff et al., 1999) allowing magma ascent without requiring upward displacements of overburden. These models predict little or no penetrative strains in the country rock.

2.3 Geologic setting of the Kern Mountains, Nevada

Previously published studies of the geology of the Kern Mountains, located near the border of Nevada and Utah (Figure 3), indicate a relatively simple history of magma intrusion to form the Tungstonia granite and penetrative deformation of surrounding carbonates to accommodate the pluton's emplacement. The Tungstonia granite is one of several Mesozoic-aged granitic intrusions of the Great Basin to the west of the Sevier Orogenic belt (Best et al., 1974; Lee et al., 1981). While core complex metamorphism and deformation are described throughout a wide-Mesozoic belt, carbonates of the Kern Mountains appear to have escaped core complex deformation (Armstrong, 1968, 1972; Barton & Trim, 1991). The Kern Mountains represent a horst bounded by large, listric basin-and-range normal faults with the Tungstonia granite at the center of the horst. The Tungstonia granite is the largest of three local intrusions, characterized by coarse muscovite and biotite grains with an emplacement age of approximately ~60 Ma based on K-Ar dating (Best et al., 1974; Lee et al., 1986).

The country rocks surrounding the Tungstonia granite consist of thick sequences of carbonate units, mostly dolostones, some limestones, and some discontinuous shales and conglomerates. Penetrative deformations and foliations in dolostones surrounding the pluton and within granite margins indicate some form of forceful emplacement (Best et al., 1974; Sayeed et al., 1977; Lee et al., 1981; Barton & Trim, 1991). Though mesoscopic indicators of shear are rare (Shea et al., 1988) the border granites (approximately ~30 m perpendicular to the contact) are heavily sheared and exhibit strong foliation (Sayeed et al., 1977). Foliations within marginal carbonates and the granite are sub-parallel (Figure 4) to the granite-country rock contact and original sedimentary stylolites are highly attenuated near the granite due to solid-state deformation and shear (Shea et al., 1988). The deformed carbonates that surround the Tungstonia granite are Late Precambrian and Paleozoic in age.

Stratigraphic studies of the country rocks of the Kern Mountains provide information about lithologies, times of deposition, and environment of deposition (Figure 5) (Drewes, 1967; Ahlborn, 1977). Most important for my study, they offer constrains on the stratigraphic column, unconformities, and depth in the crust of the Tungstonia granite at the time of emplacement. At ~66 Ma, the emplacement of the Tungstonia granite body is thought to have occurred at depths of 4-10 km (Best et al., 1974; Sayeed et al., 1977). However, stratigraphic column and erosion estimates indicate a final emplacement depth of approximately ~10.5 km by combining known strata thicknesses from published stratigraphic columns (approximately ~3.2-3.6 km) (Ahlborn, 1977) with estimates of the erosion (approximately ~7-9 km) brought on by the Sevier Orogeny, forming the Early Tertiary unconformity (Armstrong, 1968; Hose & Whitebread, 1981; Miller et al., 1983; Camilleri, 1996).

PERIOD	FORMATION/MEMBERS		THICK.
QUAT	Alluvium, L. Bonneville seds.		0-200
MIO-PLIO	High-level alluvium		0-500
	Valley fill		0-2000?
OLIG	Intermediate lavas & tuff		0-200
EOCENE	Skinner Canyon granite		intrusion
CRET	Ibapah granite		intrusion
PERMIAN	Tungstonia granite		intrusion
	Park City Grp	NULL	500
	Arcturus Formation		2000
PENN	Ely limestone		1200
MISS	Chainman sh		1100
	Joana limestone		340
DEV	Pilot sh		260
	Guilmette Formation		2300
	Simonson dolomite		700
	Sevy dolomite		800-1100
SILURIAN	Laketown dolomite		800
ORD	Ely Spring dolomite		250-400
	Eureka qtzt		200-325
	Crystal Peak dolomite		30-120
	Watson Ranch qtzt		30-150
	Pogonip	Lehmen Fm	180-300
		Kanosh sh	300-500
		Lower Pogonip undivided	1800-2000
CAMB	Notch Peak Formation		310
	Corset Spring shale		40
	Orr Formation		100-600
	Lamb dolomite		1000
	Trippe limestone		0-600
	Young Peak dolomite		500
	Abercrombie Formation		2500
	Pioche Fm	Busby qtzt mbr	500
		Cabin sh mbr	500
	Prospect Mountain qtzt		3300
pC (PROT)	G-phyllite, metasiltstone		300
	F-feldspathic quartzite		1200
	E-phyllite, quartzite		1500
	D-feldspathic qtzt		1100
	C-micaceous quartzite		1500
	B-pelitic shist		2000
	7-feldspathic qtzt		4500
	6-metasiltstone, micaceous quartzite, pelitic schist		4000
	5-metadiamictite, cg, qtzt		1200
	4-micaceous quartzite		600
	3-metasiltstone, qtzt, cg		1000
	2-marble		160
	1-pelitic		140

Figure 5. Stratigraphic column of the Kern Mountains. This stratigraphic column is for the Trout Creek area (South Deep Creek Range), approximately ~15 miles east of the Kern Mountains. Thicknesses and thickness ranges are provided in feet. The Late Paleozoic dolostones are of particular relevance to the dolostones found long the “F” traverse (modified from Hintze & Kowallis, 2009).

2.4 Experimental dolomite studies

At pressures and temperatures representative of sedimentary basins to those of the middle crust, dolomite is extremely strong (Higgs & Handin, 1959) and differential stresses generated by intrusion of melts are insufficient to deform dolomite. However, as temperatures in surrounding country rock increase due to conductive heat flow, strengths of dolomites may reduce as dislocation creep and diffusion creep are activated. Thermal softening of dolostones surrounding the Tungstonia granite may be described by activation energies of dislocation and diffusion creep. Flow laws have recently been determined for dolomite of varying grain sizes by experimental deformation studies of Davis et al. (2008), Delle Piane et al. (2008), and Holyoke et al. (2013). Dislocation creep is favored in coarse-grained dolomites with a flow law of the form:

$$\dot{\varepsilon} = A\,\sigma^{n} \exp\left(-\frac{Q}{RT}\right) \tag{1}$$

where $\dot{\varepsilon}$ is strain rate (in s^{-1}), σ is the differential stress (in MPa), the pre-exponent coefficient is A=0.079±0.1 (in $MPa^{-n}\,s^{-1}$), the nonlinear flow law is characterized by a stress exponent of n=3.0±0.1, thermal weakening is given by an activation energy of Q=148 kJ/mol, R is the universal gas constant, and T is temperature in Kelvin (Holyoke et al., 2013). Diffusion creep is the predominant deformation mechanism in fine-grained dolomites deformed at high temperatures with:

$$\dot{\varepsilon} = B\,d^{-m}\,\sigma^{n} \exp\left(-\frac{Q}{RT}\right) \tag{2}$$

where d is the grain size (in μm) with a grain size exponent, m, of 3, the pre-exponent coefficient is B=0.023±0.1 (in $MPa^{-n}\,\mu m^{m}\,s^{-1}$) (Holyoke et al, 2013), n=1.28±0.15, and

Q is the activation energy (280±45 kJ/mol) based on experiments by Davis et al. (2008), and B=10^(15±0.4), m=2.6±0.2, n=1.3±0.2, and Q=368±25 kJ/mol based on experiments of Delle Piane et al. (2008). In contrast to the nonlinear flow law for dislocation creep of coarse-grained dolomites, the flow laws reported for diffusion creep are nearly Newtonian (linear relation between stress and strain rate). However, all of these flow laws predict thermal weakening according to their respective activation energies, and the transition between dislocation and diffusion creep depends on grain size, d.

If I assume that differential stresses in the narrow deformation aureole (~70 m) surrounding the Tungstonia granite, with a diameter of ~5 km, vary little across the zone of penetrative deformation of dolostones surrounding the Tungstonia granite (i.e. stress is constant), and that strain accumulated over comparable geologic times of emplacement across the zone of penetrative deformation (i.e. temperature is constant), then the flow laws of dislocation creep and diffusion creep imply finite strain profiles that vary with temperature from the highly deformed dolostones deformed at the carbonate-granite contact to less deformed dolomites at greater distances from the contact and lower temperatures. Taking differential stress to be constant across the deformation aureole, and integrating over the same time interval (t), equations (1) and (2) lead to:

$$\varepsilon \propto C \exp(-\frac{Q}{RT}) \tag{3}$$

for dislocation creep, and:

$$\varepsilon \propto D \; d^{-m} \exp(-\frac{Q}{RT}) \tag{4}$$

for diffusion creep. Significant thermal weakening of dolostones surrounding the Tungstonia granite is implied, both for dislocation creep and diffusion creep, and measured strain profiles as a function of distance from the granite-dolostone contact can be compared with conductive temperature profiles and dependencies of strain upon temperature, as described by equations (3) and (4).

2.5 Microstructural studies of naturally deformed dolomites

Relatively few studies have been conducted to evaluate the high temperature mechanisms of deformation of dolomite at natural, geologic strain rates. Thus, this study may contribute to our understanding of dolomite deformation at varying temperatures of the contact metamorphic aureole.

Dislocation creep microstructures have been characterized in natural dolomites (Barber et al., 1977; White & White, 1980; Newman & Mitra, 1994) and compared with those of dolomites deformed experimentally at high temperatures (Neumann, 1969; Barber, 1977; Barber et al., 1981, 1994; Barber & Wenk, 2001; Davis et al., 2008; Holyoke et al., 2013, 2014). These include undulatory extinction, subgrains, and recrystallized grains at the optical scale and dislocations and subgrain walls at the transmission electron microscopy scale of observation. Deformed fine-grained dolomites show lattice preferred orientations (Newmann, 1969; Wenk et al., 1983; Leiss & Barber, 1999; Wells et al., 2014) with point maximum concentrations of c-axes that develop parallel to the shortening direction in triaxial compression experiments and appear nearly perpendicular to foliations of naturally deformed dolomites. Diffusion creep of fine-grained dolomite has been documented in a number of experimental studies (Davis et al., 2008; Delle Piane et al., 2008; Holyoke et al., 2014) and in dolomites sheared in the high temperature contact metamorphic aureole of an Alpine pluton (Delle Piane et al., 2008). Lattice preferred orientations appear to develop in fine-grained dolomite deformed by diffusion creep (Delle Piane et al., 2008) with c-axis maxima developed during simple shear, which are asymmetric and antithetic to the sense of shear.

III. METHODS

3.1 Traverse selection

The mapping efforts of several studies were considered when choosing the best traverse to collect and analyze samples. Drewes (1967), Sayeed et al. (1972, 1973), Best et al. (1974), and Ahlborn (1977) each mapped the Tungstonia pluton and surrounding lithologies and collected samples across the Kern Mountain pluton complex for various study topics (mostly for geochemical analysis of the Tungstonia granite). The base map used for this study was constructed from maps of Best et al. (1974) and Ahlborn (1977). Oriented samples collected by William "Bill" Shea and Andreas Kronenberg along traverses perpendicular to the granite-carbonate contact were prepared for optical and scanning electron microscopy, electron backscatter diffraction (EBSD) detection, and electron microprobe analyses. Foliation and lineation attitudes measured by Shea et al. (1988) in deformed dolostones surrounding the Tungstonia granite and within the granite at its margins have been adopted and plotted as a function of position at the granite-carbonate margins (Figure 4). Although the dip angles of foliations in dolostones vary, each sample traverse exhibited foliations dipping sub-parallel to the granite-dolostone contact. A traverse perpendicular to the southern margin of the granite stock (the "F" traverse of Shea et al., 1988) (Figure 6) was selected to prepare samples for study. Samples of this traverse were chosen because discontinuities due to faulting were not evident from field observations above this traverse, and evidence of shear and elongation along this traverse appear to be characteristic of the deformation aureole surrounding the

Tungstonia granite, with strain that decreases with distance from the granite-dolostone contact. Oriented sample markings were compared with field notebooks and used to reorient the samples in the laboratory, mounting them in plaster to make oriented cuts (Figure 7). All thin sections were prepared perpendicular to the predominant foliation that is parallel to the granite-dolostone contact, with one set prepared parallel to the foliation dip (approximately parallel to lineation, where it is expressed) and one parallel to the foliation strike. Oriented samples along the traverse were collected with their locations recorded relative to the granite-dolostone contact. Closest distances of these samples to the granite-dolostone contact were inferred assuming a constant dip of the contact with depth.

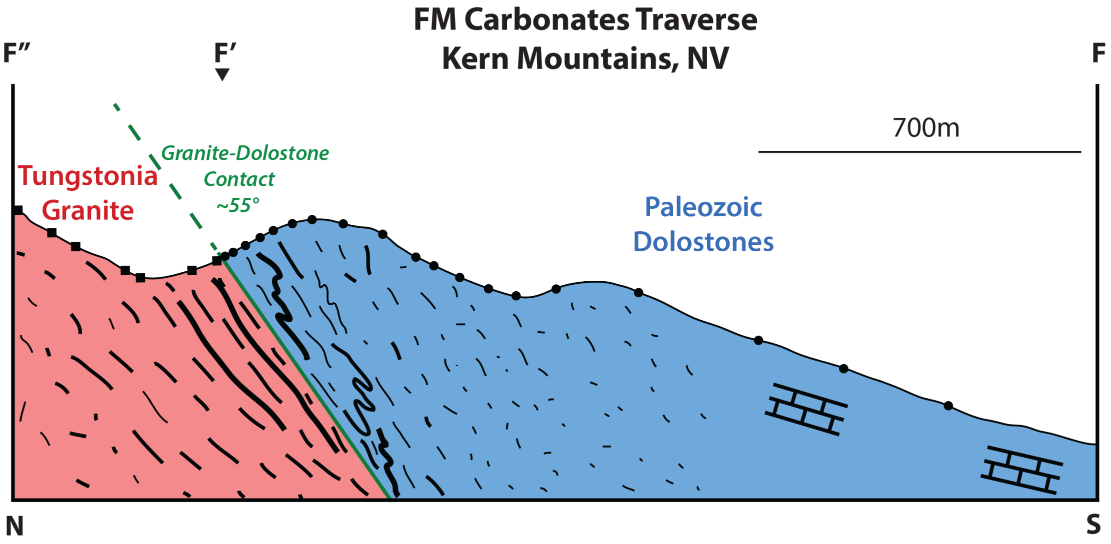

Figure 6. Profile of the "F" sample traverse, Kern Mountains, Nevada. Plotted dots (carbonates) and squares (granite) indicate where samples and foliation orientations were collected (data and profile provided by W. Shea).

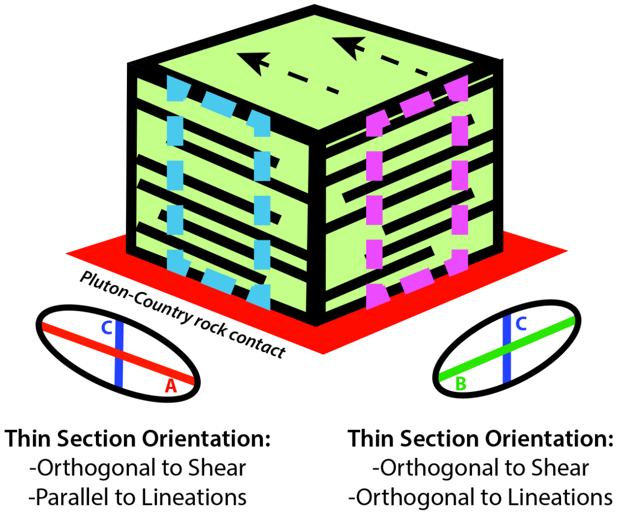

Figure 7. Orientation of dolostone thin sections. The orientations of dolostone thin section ‘cuts’ relative to the pluton-country rock contact, foliation, and lineations. Thick lines parallel to the pluton-country rock contact represent foliation and dashed lines indicate lineations. Aspect ratios for each orientation and the respective grain axis are indicated.

3.2 Microstructural study

3.2.1 Optical microscopy

The first stage of data collection began with optical microscopy of the dolostone samples to determine the following: the degree of foliation, elongation, and preferred orientation, an initial understanding of composition, and established grain size variations. These variables were combined to characterize variations in deformation and metamorphic temperatures across the traverse. Optical microscopy was also utilized to identify evidence of deformation in marginal granite samples, to compare their deformation qualitatively with deformations in the surrounding dolostones, to identify minerals for compositional analyses, and to map areas on thin sections that required scanning electron microscopy imaging and electron backscatter diffraction (EBSD) analysis.

3.2.2 SEM microscopy and EBSD detection

Grain shapes and sizes were determined from scanning electron microscope (SEM) images, using both secondary electrons (SE) and backscattered electrons (BSE), which grain boundary imaging allowed unambiguous identification of grain boundaries. EBSD detection was performed to determine lattice-preferred orientation (LPO) due to penetrative deformation. Kikuchi bands observed by EBSD detection were analyzed for crystal orientation using software in the HKL Channel 5 suite (Oxford Instruments). EBSD detection was performed on a FEI Quanta 600 FE-SEM at an accelerating voltage of 30 kV with a beam current of 10 nA, a spot size of 5, and a working distance of 17 mm.

After the deformation microstructures and LPOs were characterized for each sample, the data were compiled, comparing results for each pair of oriented thin section, crystallographic c-axes, a-axes, and poles to r {10-14} and poles to f {01-12} were plotted using the Channel 5 Suite program Mambo. Stereonets with these LPOs allowed further interpretation of the relationship between intensity of shear and distance from the intrusion, as well as determining the symmetry or asymmetry of shear. LPO intensities exposed by the dolostones were also used as a qualitative proxy for intensity of penetrative strain. In addition to the aspect ratios and resulting Flinn diagrams, the LPO of the dolostones were compared with LPOs measured in experimentally deformed dolomites and other naturally deformed dolomites, comparing the LPO patterns and asymmetries relative to foliation and shear direction. A cone angle of 12 was chosen to contour crystallographic axis distribution so that contours are equivalent to Kamb contours for N, the number of grains measured in each sample, of 400+ grains per sample (Kamb, 1959).

3.3 Electron microprobe: BSE imaging and compositional analyses

Backscatter Electron (BSE) imaging and compositional analyses were carried out on a four spectrometer Cameca SX50 electron microprobe at an accelerating voltage of 15 KV, beam current of 10 to 50 nA, and a beam diameter of 10 μm. Double-polished thin sections were coated with ~15 nm of high purity carbon (for compositional analysis) and later increased to ~50 nm (for high beam-current BSE imaging) prior to analyses to eliminate charging. BSE imaging conditions were run in atomic number mode at an accelerating voltage of 15 kV and a beam current of 10 nA using a 6-component BSE detector. Additionally, I searched through the thin sections for secondary and metamorphic minerals using energy dispersive spectroscopy (EDS) and BSE imaging to map for future compositional analyses. All compositional analyses were performed using WDS (wavelength-dispersive) X-ray spectrometers to characterize compositions of all secondary minerals of samples that coexist with the primary phase, dolomite, with the goal of constraining temperatures of deformation. Analyses were carried out after standardization using well-characterized compounds or pure elements; standard checks were run to verify standardizations.

The high-resolution images of dolomite grains I captured were traced using Adobe Illustrator to analyze the grain shape, size, and shape-preferred orientation of 200+ dolomite grains per sample. The major and minor axes of dolomite grains parallel and perpendicular to the plane of foliation, respectively, in the two orthogonal sections were measured and the major axes, A and B, in the two sections were normalized by the minimum axis, C, which is captured in both orthogonal sections (Figure 7). The grain shape ratios (A/C) and (B/C) were used to characterize strains due to intragranular deformation mechanisms and illustrated on Flinn diagrams of the 3-Dimensional strain ellipsoid. Clearly any strains associated with grain boundary processes of diffusion creep and/or grain boundary sliding are not recorded by this method, and only minimum finite strains can be recorded following any dynamic recrystallization. Thus, it must be realized that grain shapes do not indicate total strain; rather, they may only represent a fraction of the accumulated strain.

3.4 Mineral equilibria and phase diagrams

Upon the identification of metamorphic minerals and completion of compositional analyses, the mineral equilibria were determined so that phase diagrams could be constructed to constrain temperatures at a given pressure. Mineral analyses were normalized for oxygen and then on a cation basis: all carbonates to 2 cations, diopside to four cations, tremolite to 13 cations, and clinochlore to 10 cations. The resultant mineral activities help restrict the temperature and fluid composition depending on the various mineral assemblages present across the traverse. Phase diagrams were generated (via the program Thermocalc) for each sample at minimum and maximum estimated pressures (300-400 MPa). Peak temperature constraints were determined for all samples; however, minimum temperature constraints for several samples could not be established due to lack of restrictive mineral assemblages.

Metamorphic phases and calcite exhibiting evidence of non-equilibrium were not considered for phase equilibrium analysis. More specifically, secondary grains found in veins, which may have arrived after emplacement via fluids, or exhibiting rimming/zoning were not considered to be in equilibrium with surrounding dolomite. Potential indicators of equilibrium by metamorphic minerals include being surrounded by dolomite grains that do not exhibit zoning and shape-preferred orientation sub-parallel to that of the dolomite.

3.5 Calcite-dolomite geothermometry

In addition to constraints placed on contact metamorphic temperatures by phases present in the dolostones, calcite compositions were measured (via compositional analysis on the electron microprobe) with the goal of estimating peak temperatures during granite emplacement using the calcium-magnesium ratio of calcite grains that coexist with dolomite. Magnesium compositions (XMg) were calculated from mineral analyses and applied to an equation that quantifies the peak temperature as defined by the calcite-dolomite solvus created by Anovitz and Essene (1987). This solvus was chosen over others (Goldsmith et al., 1962 and Rosenberg, 1972) because proper reversal techniques were applied and it accounts for iron and manganese in the cation sites (Letargo et al., 1995).

3.6 Evaluation of temperature gradient

A simple 1-Dimensional heat flow model was used to fit estimates of peak temperatures of samples along the traverse and solutions in Turcotte and Schubert's (2002) text to estimate cooling times over which the Tungstonia granite was emplaced. Additional constraints to 1-D heat flow came from the solidus temperature of the two-mica Tungstonia granite, assuming its stability at 350+ MPa based on muscovite equilibrium at depth (Evans, 1965), and estimates of temperature far from the granite, assuming a normal continental geothermal gradient.

The strain and temperature profiles were compared with published forceful emplacement models and used to test intrusion mechanisms. Additionally, symmetry/asymmetry of crystallographic-preferred orientation (CPO) plots and evidence for pure shear, simple shear, and sense of shear were characterized. These combined findings helped to confirm the mechanism for emplacement; while magmatic diapirism is expected to result in asymmetric fabrics, dominated by simple shear, ballooning is expected to result in symmetrical fabrics associated with pure shear (Holder, 1979; Marsh, 1982). It should be noted that a mixture of the two mechanisms could be present, which is entirely possible given that both mechanisms exhibit similar sharp contacts and contact-parallel foliations.

The results of this study were also used to test the flow law of dolomite at the natural strain rates associated with forceful emplacement of the Tungstonia pluton and compared with flow laws determined experimentally at high strain rates or dislocation and diffusion creep (Davies et al., 2008; Delle Piane et al., 2008; Holyoke et al., 2013).

IV. RESULTS

The average grain size, average grain shapes, and distances perpendicular to the granite-dolostone contact have been measured (Table 1). Further microstructural observations and measurements of strain, crystallographic orientations, and mineral compositions provide the basis for analysis of the emplacement mechanism.

4.1 Petrographic and microstructural observations

Carbonate rocks surrounding the Tungstonia granite are composed of nearly pure dolomite (~80-95%) with trace amounts of other minerals, including quartz, calcite, phlogopite, tremolite, muscovite, clinochlore, anorthite, and biotite. Given the disequilibrium implied by silica-rich fluids of the granite and carbonates, few skarn-type minerals are observed, apparently like fluid transport (Nyman et al., 1995). Grain sizes of the dolomites vary from fine-to medium-grained, and grain shapes vary with distance from the contact. Grain shapes and their alignment correspond closely to the foliations measured in hand specimens, with grain shape preferred orientations that are subparallel to the shear plane of the granite-dolostone contact and maximum extensional grain strains are parallel to the down-dip direction, which corresponds to the lineation, where it is expressed. This foliation is present up to 400 m orthogonal to the contact and weakens with increasing distance from the pluton. Dolomite grains closest to the intrusion (from the granite-dolostone contact to ~30 m away) are subrounded, elongate within the foliation plane (average aspect ratios range from 1.35-2.22), and feature

SAMPLE	***Distance ⊥ granite-dolostone contact (m)***	***Number of grains measured***	***Mean grain size (μm)***	***Mean grain shapes (A/C)***	***Mean grain shapes (B/C)***
FM-1	4	248	73	1.85	1.41
FM-2	17	224	36	1.35	1.65
FM-3	30	220	49	2.22	1.83
FM-4	51	208	90	2.28	2.07
FM-5	69	205	76	1.93	2.12
FM-6	93	204	157	1.50	1.47
FM-7	117	211	87	2.30	2.13
FM-8	160	207	64	2.37	2.31
FM-9	211	204	53	2.16	1.75
FM-10	277	210	34	1.61	1.82
FM-11	310	208	52	2.03	2.30
FM-12	348	204	59	1.54	1.57
FM-13	387	208	35	1.93	1.85
FM-14	439	202	123	1.03	1.03
FM-16	698	222	15	1.22	1.20

Table 1. Positions and measurements of Kern Mountain dolomite. Distances perpendicular to the granite-dolostone contact were determined from cross section viewing assuming a constant dip angle of 55°. Mean grain sizes were established for ellipsoidal grains with equivalent volume to a spherical grain and reported as grain diameters in microns.

triple-point grain boundaries (Figure 8a). The average grain size of dolomite in these rocks ranges from 35-73 μm (Figure 9) with intermittent aggregates of larger dolomite grains (~100-400 μm) parallel to foliation. Also, weak-to-moderate undulatory extinction is common, especially in grains larger than ~70 μm (Figure 8b). Dolomite grains from ~30 m to 698 m away from the pluton are angular-to-subrounded, very elongate (average aspect ratios range from 1.50-2.37), and exhibit a strong shape-preferred orientation that decreases with distance from the pluton (Figure 8c). Average grain sizes range from 34-90 μm, with the exception of FM-6 (~93 m from the contact with an average grain size of 157 μm) and FM-14 (~440 m from the contact with an average grain size of 123 μm), and are occasionally bimodal with a secondary grain size of ~70-100 μm. Aggregates of large dolomite grains are more common throughout this interval (especially ~51 m to ~69 m from the contact) and are oriented parallel to foliation, with serrated and lobate grain boundaries and twinning typical (Figure 8d). Core and mantle structures are present in this interval consisting of mantles made up of very small dolomite grains (~10-30 μm) in thin (~30-60 μm) zones that surround cores made up of large grain aggregates. Undulatory extinction is also present, though most common in large grains (~70+ μm), but decreases in occurrence with increasing distance from the pluton and is no longer present farther than 160 m from the pluton. Compositional foliation of silicate minerals (e.g. tremolite) is common in samples ~30-160 m from the contact as they are aligned parallel to foliation of dolomite grains (Figure 8e). Dolomite grains farther than 698 m from the pluton are rounded with near

Figure 8. Microstructures and textures of dolomite grains in proximity to the Tungstonia granite. (A) Dolomite grains are subrounded, elongate, and foliated from the granite-dolostone contact to ~51 m away (shown here: ~17 m from the contact). Triple-point grain boundaries are very common; (B) Undulatory extinction, seen here in FM-1 (~4 m from the contact), is present in dolomite from to the granite-dolostone contact to ~160 m away; (C) Dolomite grains are subangular to subrounded from ~51 m to 698 m from the pluton. Grains are more elongate and exhibit a stronger sense of shape-preferred orientation from the pluton (shown here: ~69 m from the contact) than dolostones closer to the intrusion. Triple-point grain boundaries are absent from this interval; (D) Twinning and serrated grain boundaries are most common in the largest grains (100-500 μm); (E) Silicate minerals (e.g. tremolite) are present in samples up to 117 m from the granite-dolostone contact and are aligned parallel to the shape preferred orientation of dolomite; (F) Dolomite grains in Sample FM-17 (~823 m from the contact) are rounded with random orientations and appear to be "dirty" or have defects within grains. Sedimentary textures are common 698+ m from the granite-dolostone contact.

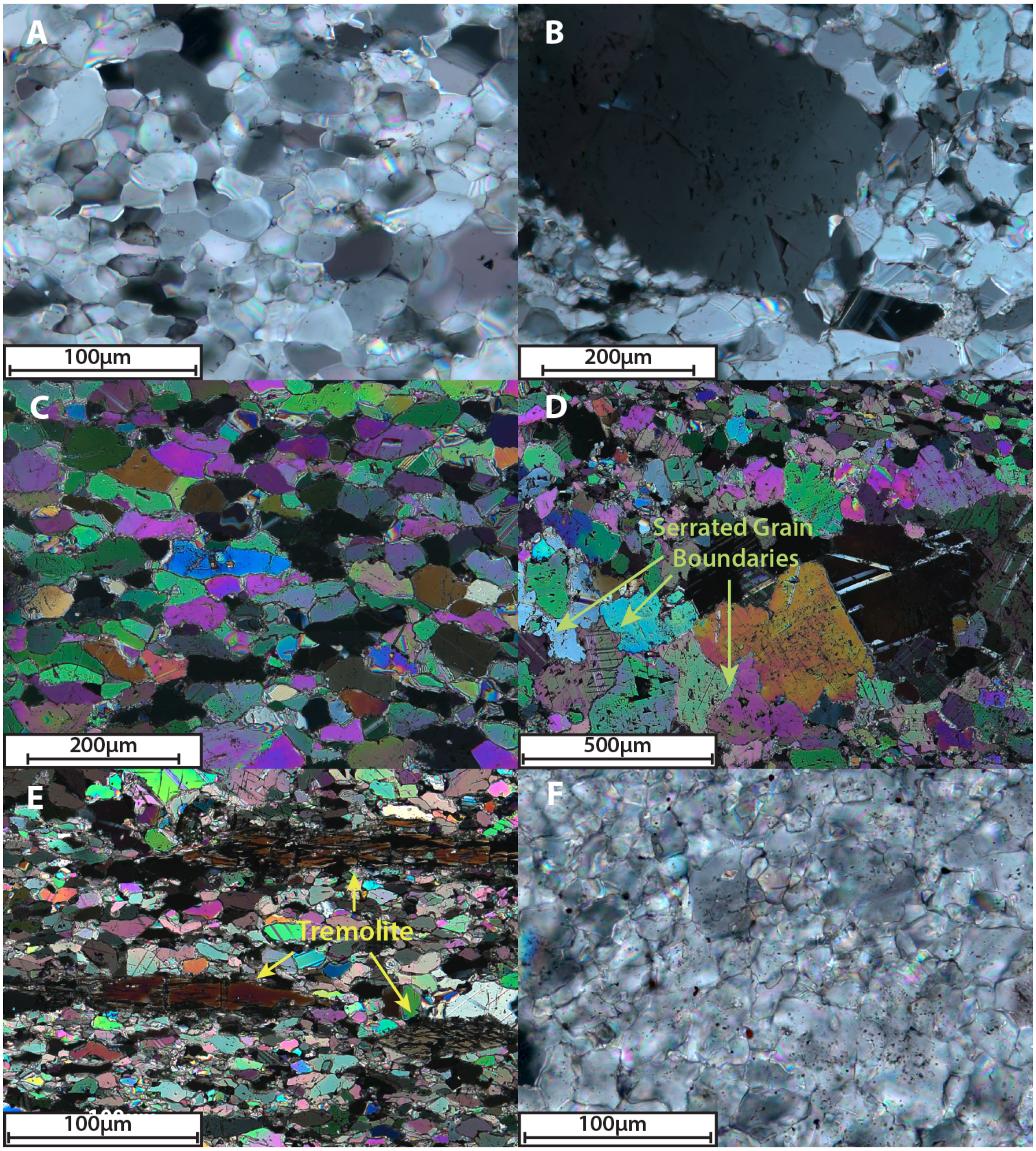
A
100µm
B
200µm
C
200µm
D
Serrated Grain Boundaries
500µm
E
Tremolite
100µm
F
100µm

equant axial ratios (average aspect ratios range between 1.01 to 1.21) and show no evidence of deformation (Figure 8f).

4.2 Grain shapes and inferred grain strains

Based on measured aspect ratios (A/C) and (B/C) in two orthogonal thin sections for each sample (Table 1) and normalized measurements of C in both sections, I have inferred grain strains in a common reference frame defined by the foliation and lineations. Intragranular finite strains ε_1, ε_2, and ε_3 determined from grain shapes are plotted with distance from the intrusion where distances were determined from sample positions and dip of the granite-dolostone contact (Figure 10). Shortening strains (considered positive) are perpendicular to the foliation and granite-dolostone contact up to 400 m away with an average strain of 40%. Grain strains are extensional (considered negative) within the plane parallel to foliation and maximum elongations correspond to the down-dip lineation direction, with a few exceptions, along the traverse to distances of ~400 m away. Strain along this plane ranges from 15-50% elongation; however, a few samples indicate shortening as high as 20%. A significant drop off in strain along all three axes occurs approximately ~387 m from the granite-dolostone contact. In addition, the log values of aspect ratios parallel to lineations (A/C) and perpendicular to lineations (B/C) were plotted (Figure 11) and create a linear trend that coincides with the trend of plane strain.

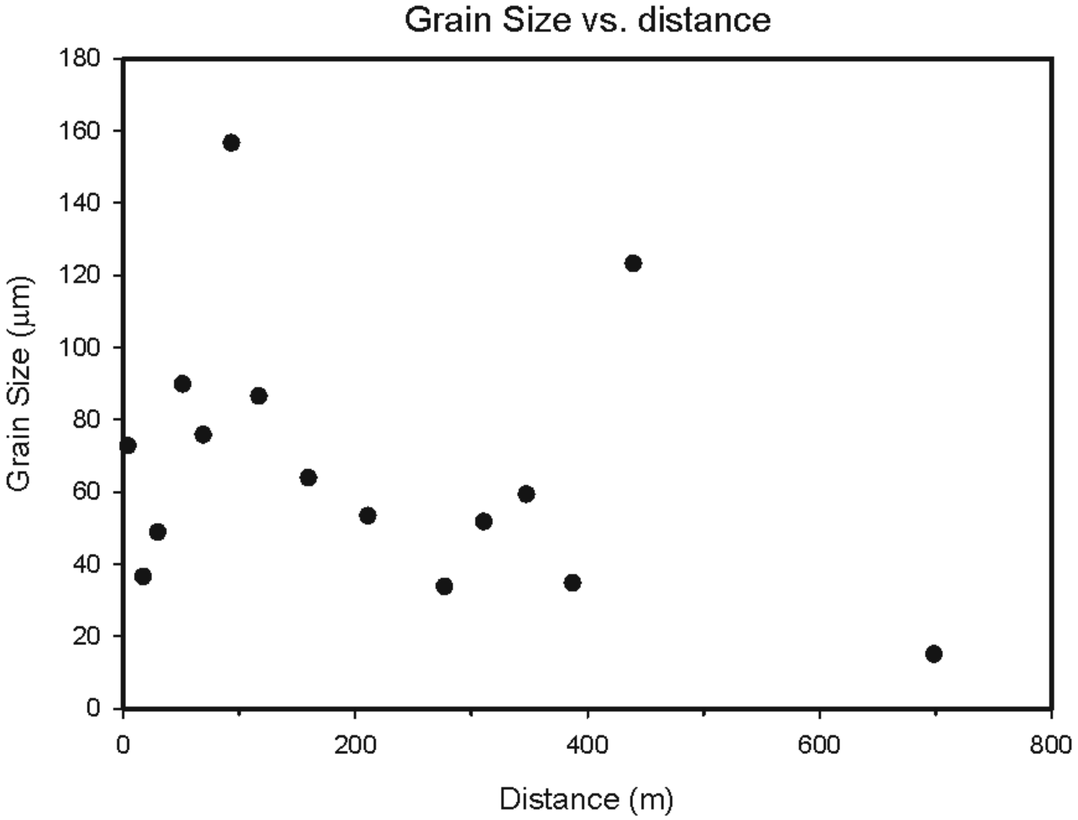

Figure 9. Dolomite grain size vs. distance. Measured grain size of dolomite grains across the "F" traverse of the Kern Mountains as a function of distance form the granite-dolostone contact determined in cross section.

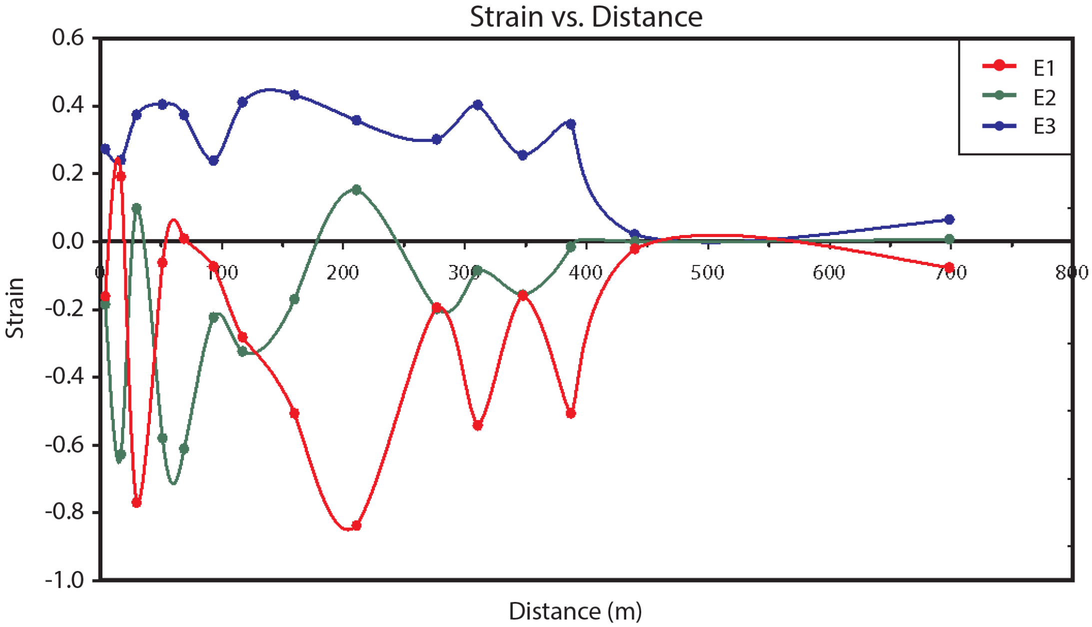

Figure 10. Inferred strain vs. distance. Inferred intragranular strains of dolomite as a function of distance from the granite-dolostone contact, as determined in cross section. E1 (red) represents the strain parallel to lineations, E2 (green) represents the strain perpendicular to lineations, and E3 (blue) represents the strain of perpendicular to foliation. Positive values indicate shortening and negative values indicate elongation.

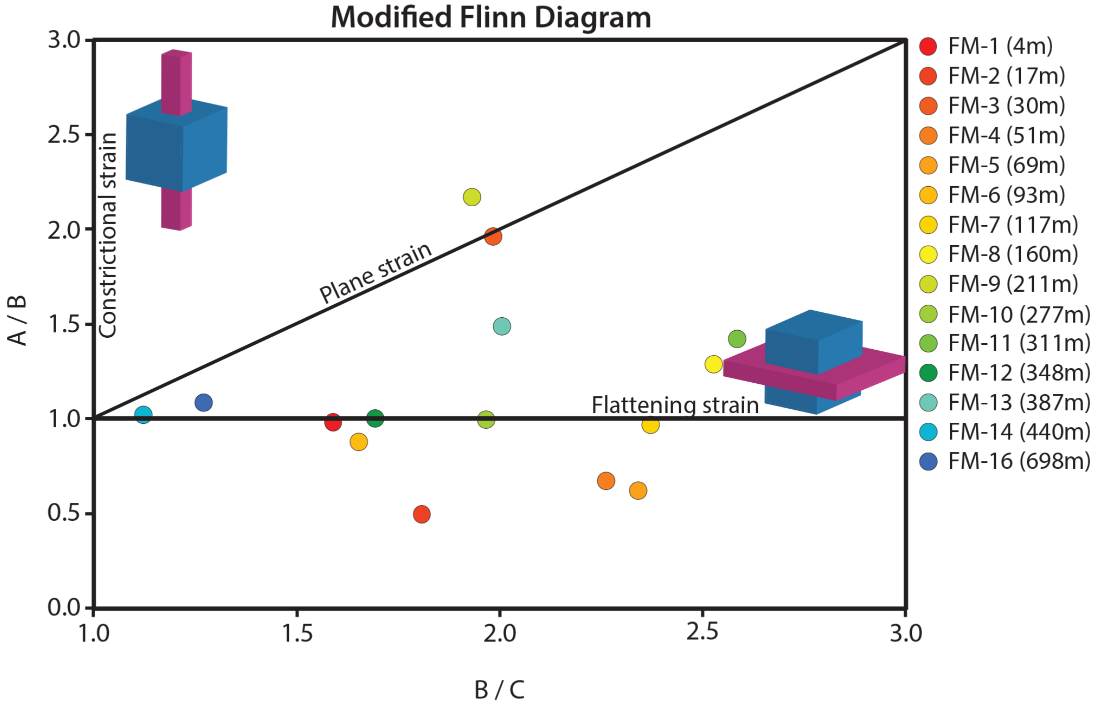

Figure 11. Modified Flinn diagram. This modified Flinn diagram shows the aspect ratios A/B and B/C representing a 3-D strain ellipsoid of dolomite grains. The plotted strain data are in agreement with a combination of plane strain (solid line) and flattening strain across the "F" Traverse. The color of each sample reflects its proximity to the intrusion (red dots are closest to the intrusion; blue dots are furthest from the intrusion).

4.3 Crystallographic orientations of dolomite

Crystallographic c-axes of dolomite near the granite-dolostone contact exhibit point maximum concentrations at high angles (~65°-80°) to foliation, with concentrations that decay with distance from the contact (Figure 12). C-axis concentrations reach values of ~2.8 to 3.6 times the expected concentration for a random distribution. Corresponding a-axes form a diffuse girdle that reaches values of ~2.0 to 2.5 times random distribution perpendicular to the c-axis maxima, and roughly coincident with foliations and the granite-dolostone contact orientation. These LPO patterns are systematically asymmetric with respect to foliation with c-axis maxima that are closer to vertical (larger plunge angles) than the normal to foliation. Notably, LPO patterns become diffuse by 50 m distance from the granite-dolostone contact, even though grain shapes indicate plane strain out to distances of ~400 m. Little or no preferred orientations are apparent in the poles to r or poles to f (which represent potential slip and twin planes of dolomite).

4.4 Metamorphic aureole and constraints on peak temperatures

While the dolostones surrounding the Tungstonia granite are nearly pure dolomite, thorough EDS searching has been useful to locate trace minerals within the dolomite host that may be used to constrain peak temperatures of metamorphism (Table 2). Calcite is present in several samples and calcite-dolomite geothermometry of these in-equilibrium grains allow for temperature constraints (Figure 13). The highest peak temperatures are found within ~93 m of the pluton contact and decrease with increasing distance from the intrusion.

In-situ conditions, mainly pressure and initial temperature of country rock prior to intrusion (background temperature) were estimated, based on stratigraphic and petrologic constraints on pressure and an assumed continental geothermal gradient. In-situ pressures are estimated to be 300-400 MPa based on the reconstructed stratigraphic column and additional petrologic constraints of muscovite equilibria, which have a minimum pressure limit of ~3.5 kbar, for the Tungstonia granite (Kerrick, 1972). Background temperatures at depth are estimated to be 235°-287°C based on geothermal

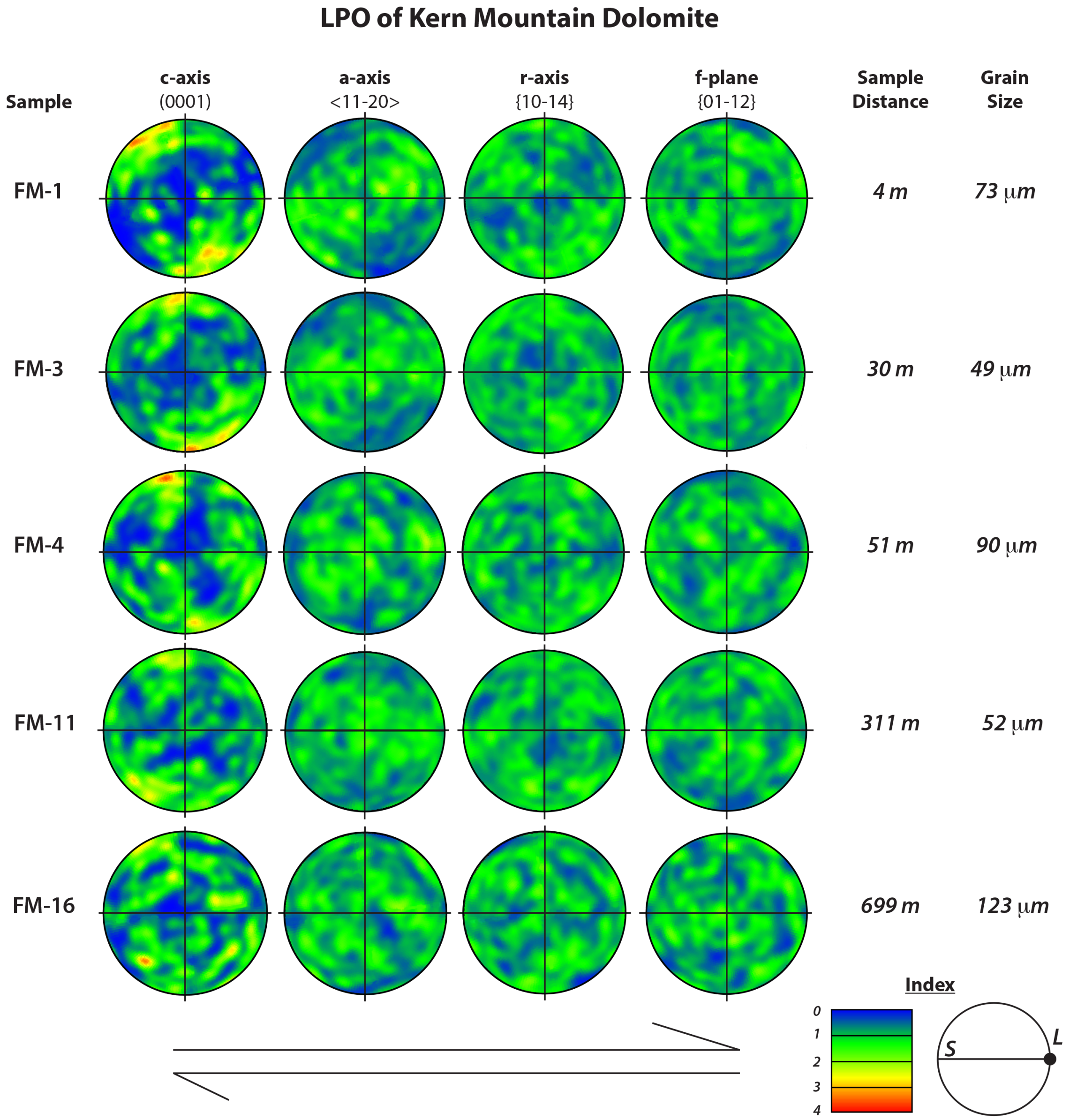

Figure 12. CPO of Kern Mountain dolostones. Orientations of crystal lattices obtained from EBSD and analysis of mineral Kikuchi bands in dolomite grains from the Kern Mountain dolostones are plotted in these lower hemisphere equal-area stereographic projections. Samples closest to the intrusion (up to ~55 m away) exhibit point maximum concentrations with c-axes sub-perpendicular to the foliation plane and a girdle trend along the a-axis subparallel to the shear plane. C- and a-axis concentrations are asymmetric with c-axis maxima that have higher plunge angles than foliation. At distances farther than ~55 m from the pluton no discernible patterns or trends of point concentrations are detected in any of the listed orientations. The orientation of foliation (S) and lineations (L) are indicated. The maximum contour is 4.

Sample *(dist. in m)* **Mineral** Activity	**FM-1** *(4m)*	**FM-2** *(17m)*	**FM-3** *(30m)*	**FM-4** *(51m)*	**FM-5** *(69m)*	**FM-6** *(93m)*	**FM-7** *(117m)*	**FM-8** *(160m)*	**FM-9** *(211m)*	**FM-10** *(277m)*	**FM-11** *(310m)*	**FM-12** *(348m)*	**FM-13** *(387m)*	**FM-14** *(439m)*	**FM-16** *(698m)*
Dolomite	0.99	0.99	0.99	0.99	0.99	0.99	0.99	0.96	0.99	0.98	0.99	0.99	0.99	0.99	0.99
Calcite	**X**†	0.86	0.90		0.85	**X**†	0.98*	0.95	0.98	0.98*	0.97		0.87*	0.93*	0.82*
Phlogopite				**X**†	**X**†	0.30	0.29	0.42	0.29	0.34	0.29		0.35		
Tremolite					0.32		0.26								
Quartz	**X**		**X**	**X**	**X**	**X**		**X**	**X**		**X**	**X**			**X**
Anorthite	0.93														
Chlinochlore							0.99		0.96						
Muscovite	0.44	0.26	0.54	0.45	0.40	0.31	**X**†			0.47	0.47	0.53	0.39	0.49	0.41

Table 2. Mineralogical compositions and average activities of the Kern Mountains dolostones. Mineral presence within a sample is indicated with the average calculated activity of that mineral or with X† to indicate mineral presence, but unable to gather quality data (mainly due to small grain sizes). Calcite activities labeled with an asterisk indicate calcite present in veins. Quartz presence is indicated with an X because quartz activities were not calculated.

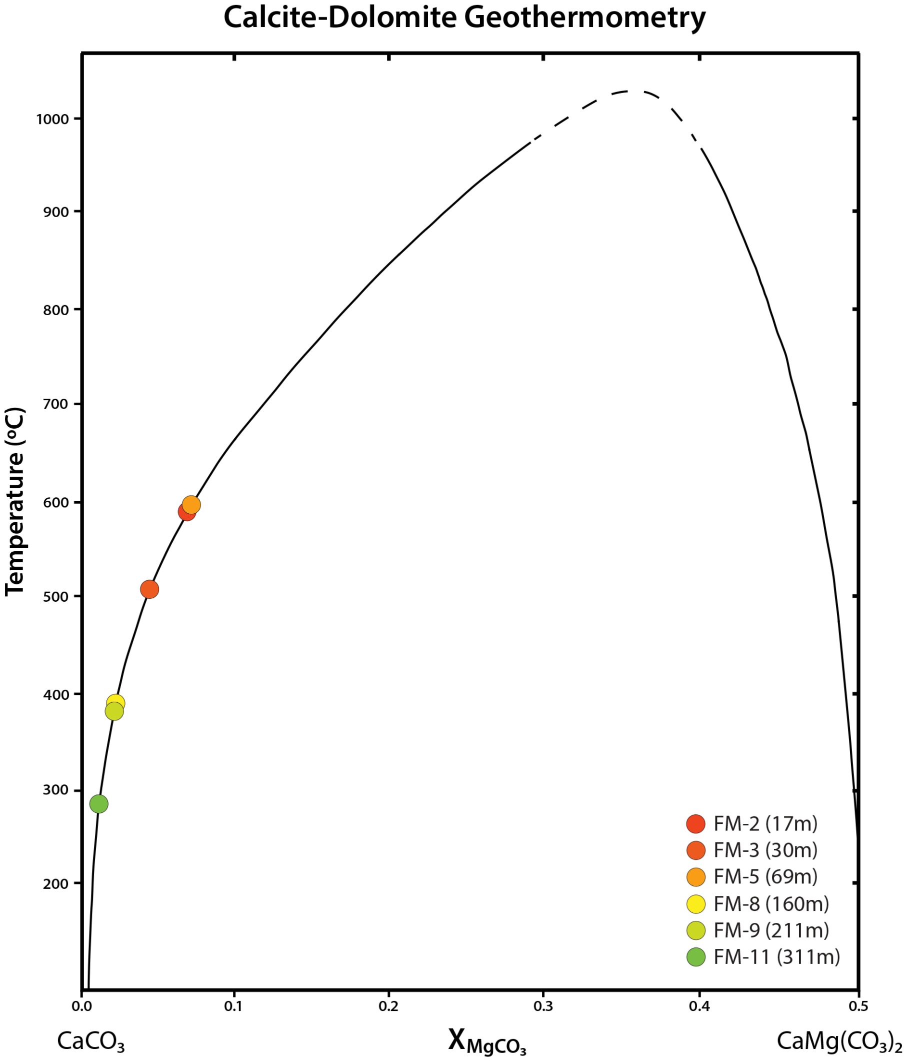

Figure 13. Calcite-dolomite geothermometry. Temperature values were calculated via calcite-dolomite geothermometry and plotted on the calcite-dolomite solvus published by Anovitz & Essene (1987). Temperatures of the calcite from the Kern Mountain dolostones generally decrease with distance from the contact; however, FM-5 exhibits a higher temperature than samples closer to the intrusion (modified from Anovitz & Essene, 1987).

Mineral equilibria calculated from compositional analyses of silicate phases, dolomite, and calcite grains allowed for the construction of temperature-X$_{CO2}$ phase diagrams for each sample (Figure 14) from which peak temperature could be estimated. In addition, minerals (e.g. talc, microcline, and diopside) not present within the Kern Mountain dolostones were added to help produce restricting reactions for each sample. Several samples have limited mineral assemblages (for example: dolomite + quartz + muscovite) that suggest no reactions take place; however, by adding a mineral not actually present (e.g. diopside), a maximum/minimum temperature can be estimated based on the T-XCO_2 conditions of the real assemblage (so the equation dolomite + quartz = diopside + CO_2 would provide a maximum temperature constraint because diopside is in equilibrium at higher temperatures but is not in the sample). Because higher pressures will generally yield higher possible temperatures for reactions, maximum temperature constraints are assumed based on the highest temperature present at 400 MPa for each sample. Conversely, the minimum temperature constraints are assumed based on the lowest temperature present at 300 MPa for each sample. The temperature ranges vary depending on the mineral reactions for each sample, and, for several samples, only an upper temperature limit could be determined due to less varied mineral assemblages. The temperature constraints from mineral phase diagrams, calcite-dolomite geothermometry data, and published peak temperatures of the Tungstonia granite indicate a temperature profile (Figure 15) with a narrow high temperature window (background temperatures are realized at ~387 m from the pluton).

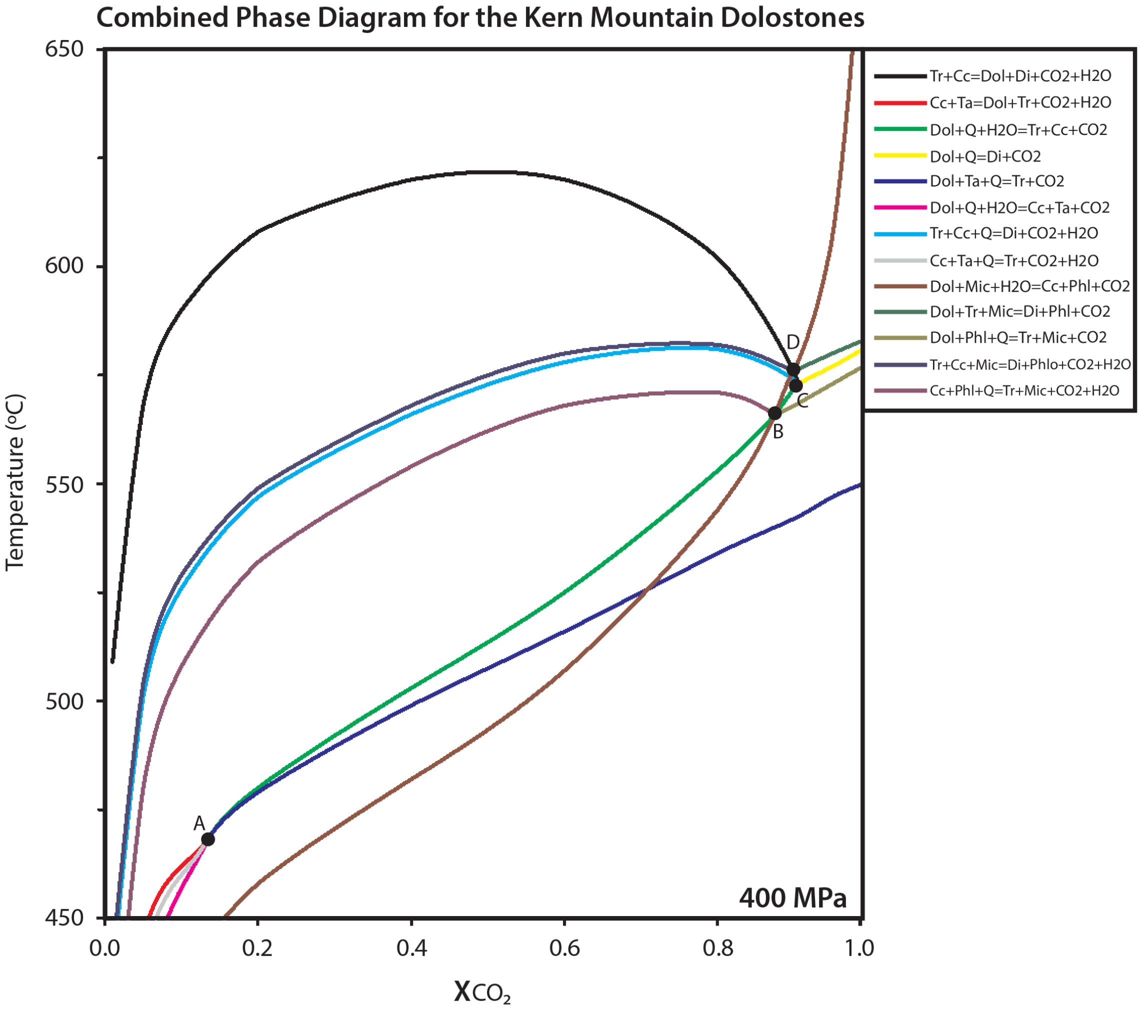

Figure 14. Combined phase diagram for the Kern Mountain dolostones. This is a representative temperature-XCO_2 phase diagram for the Kern Mountain dolostones at 400 MPa assuming an ideal model (activities for all minerals on the plot are 1.0). All restrictive mineral assemblages are represented. Invariant point A = calcite + dolomite + quartz + talc + tremolite; Invariant point B = dolomite + calcite +quartz + tremolite + microcline + phlogopite; Invariant point C = calcite + dolomite + phlogopite + tremolite + diopside + microcline; Invariant point D = calcite + dolomite + quartz + tremolite + diopside. For abbreviations, see the nomenclature section.

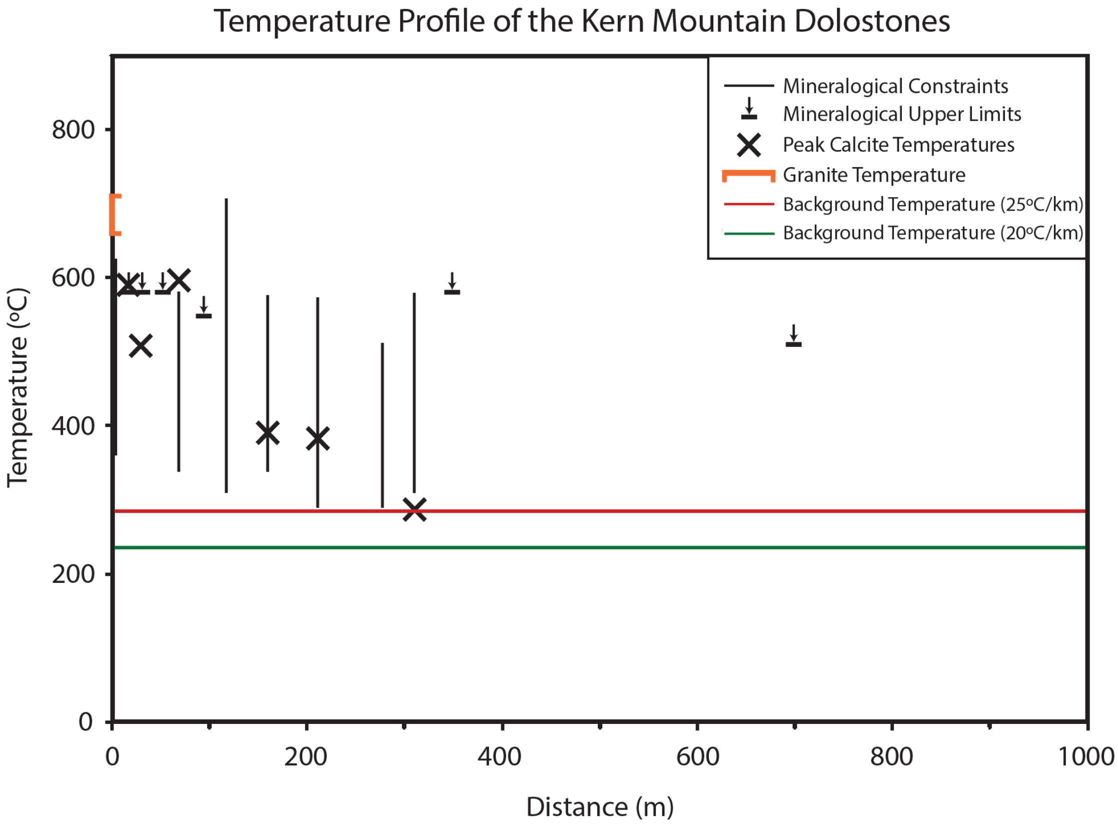

Figure 15. Combined temperature profile for dolostones along the “F” traverse of the Kern Mountains. The classification for each temperature constraint method is shown in the legend. The temperature range for the Tungstonia granite was determined by previous studies (Sayeed et al., 1977).

V. DISCUSSION

Previous work has indicated that a strain rate-temperature relationship defines dolomite rheology (Davis et al., 2008; Delle Piane et al., 2008; Holyoke et al., 2014). Based on the findings of this study, a strain rate-temperature relationship is confirmed consistent with mechanisms of magma emplacement by thermal weakening and nonlinear flow of dolostones surrounding the Tungstonia granite.

5.1 Temperature vs. distance

Basic field observations of dolostones surrounding the Tungstonia granite imply relative narrow widths to the metamorphic and deformation aureoles. Estimates of peak metamorphic temperatures (Figure 15) confirm the narrow metamorphic aureole and initial heat-flow modeling suggests a short duration of heating. A simple, one-dimensional (1-D) time-evolving heating problem (Turcotte & Schubert, 2002; pgs. 149-159; see Appendix) was applied:

$$\mathrm{T} = \mathrm{T_m} - (\mathrm{T_m} - \mathrm{T_0})\,\mathrm{erf}\left(\frac{\mathrm{x}}{2\sqrt{\kappa\,\mathrm{t}}}\right) \tag{5}$$

where T is temperature (in °C), T_m is the temperature of the magma body (in °C), T_0 is the initial (background) temperature of the host rock (in °C), x is the distance from the pluton (in meters), κ is the diffusivity constant (in m^2 $years^{-1}$), and t is elapsed time of heating (in years). Based on this model (Figure 16), the time over which heat was exchanged was only ~100-2,200 years, which is surprisingly short considering this model also ignores latent heat that would increase the duration of conductive heating.

Assuming that the pluton was emplaced as a spherical intrusion, there must be large amounts of energy (heat) emitted given the established melt temperature of the Tungstonia granite (680°-710°C) (Sayeed et al., 1977). If the transfer of heat extended out to only ~300 m from the edge of the granite, then approximately 75% of the expected energy (heat) output is unaccounted for (not including latent heating from the "tail" of the intrusion). Much of the heat lost from the granite may have been lost above its eroded top, possibly by hydrothermal convection (Spera, 1980). Indeed energy balance considerations suggest that lateral heat flow in the rocks exposed along the margins of the Tungstonia granite represent only a small fraction of total heat flow for the entire magma body. Another possible explanation is that the dolostones observed were not close to the intrusion at the time of emplacement. High temperatures should have transferred much farther than 300 m away from the granite-dolostone contact, so a 1-D conductive cooling problem indicates movement of heat out of the plane of 1-D.

Nevertheless, a number of key observations of rocks surrounding the Tungstonia granite indicate that lateral heat flow was by heat conduction rather than convective heat transfer and that cooling times were short (<2,200 years). The lack of significant skarns along the margins of the Tungstonia granite and the disequilibrium of silica-rich fluids of the magma body and surrounding carbonates suggests very little fluid transport. Compositionally unaltered carbonates are relatively common around many silicate minerals and this has been taken as evidence for very low permeabilities to fluids in carbonates that are deformed at high temperatures by ductile creep processes. Low permeabilities of the dolostones surrounding the Tungstonia granite may explain the few calc-silicate minerals observed (and the difficulty to estimate temperatures). It simplifies my analysis of dolomite creep, but most of the heat lost from the pluton must have escaped elsewhere, possibly at the top. Although this model does not constrain emplacement times well, it does indicate that a more complex thermal model must be constructed in order to establish the duration of emplacement.

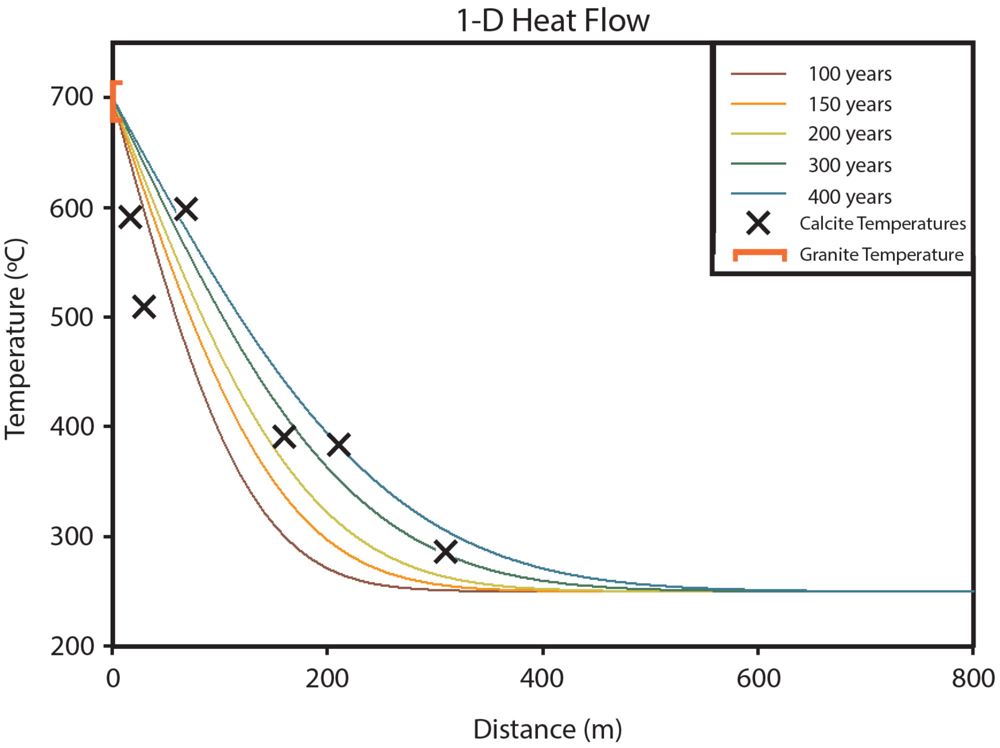

Figure 16. Simple thermal model attempt. 1-D time-evolving heating problem that shows heating curves at five different times assuming constant heat flow. This illustrates the problem with assuming a simple thermal model: the temperature profile indicates that heating should have occurred over the course of <2,200 years. These heating/emplacement times are very fast and unlikely.

5.2 Strain rate vs. distance

5.2.1 Inferred strain rates

Strain rates of dolostones surrounding the Tungstonia granite were estimated from inferred grain strains and the estimate of emplacement times derived from 1-D heat flow (~100 years to 2,000 years). Much like the measured strains (Figure 10), calculated strain rates along the compressional axis produce a strain rate plateau (Figure 17) with strain rates of approximately ~10^{-10} s^{-1}. The difference in strain rates between the two series shown reflects the emplacement times and could be further constrained by more complex thermal models. One point to consider is if strains were larger than those measured in the 30 m section adjacent to the intrusion. The expected trend for strain was for the highest values to be immediately adjacent to the intrusion and decrease with increasing distance from the pluton, not a strain plateau out to 400 m away. Those samples that recrystallized may have had greater strains than were measured, as high strains are limited by recrystallization. Conversely, low measured strains (<0.05) may not be dependable due to the difficulty of accurately measuring strains that small. It is possible that high temperatures, small grain size, or a combination of both could have activated diffusion creep, which would have presumably removed evidence of larger strain; however, there is no way to prove this occurred.

5.2.2 Strain rates predicted from flow laws

Given measurements of temperature, T, and grain size, d, and estimates of differential stress, σ, for the Kern Mountains dolostones and the A, n, m, and Q values reported for dislocation creep and diffusion creep (Davis et al., 2008; Holyoke et al.,

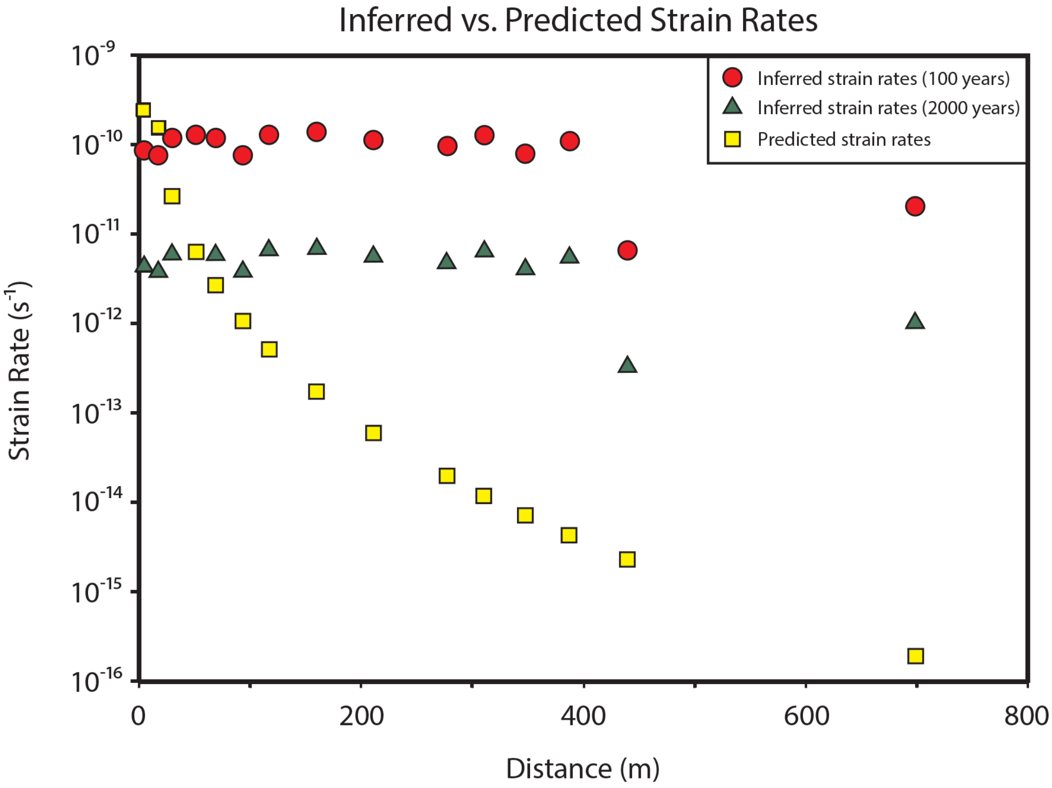

Figure 17. Comparison of strain rates from both methods. Strain rates determined from measured strain compare favorably with predicted strain rates within the time constraints calculated from simple thermal models until ~117 m from the pluton. Predicted strain rates for dolostones farther than 117 m from the pluton become slower than strain rates within the time constraints.

2013), inferred strain rates can be compared with predictions based on dolomite flow laws. In order to determine the predicted strain rates due to dislocation creep and diffusion creep, assumptions of granite melt density of 2.55 g/cm^3 (Best, 2003), average host rock density of 2.7 g/cm^3 (Ahlborn, 1977; Hintze & Kowallis, 2009), intrusion source depths of 10-20 km deeper than final emplacement depth (20.5-30.5 km) (Lee & Christiansen, 1983; Miller & Gans, 1989), and a constant stress and magma pressure indicate a differential stress of 27.8-55.6 MPa (Figure 18), which when combined with measured temperature values from the field allow for constraints on the conditions for the Kern Mountains.

Upon reflection of comparison, the strain rates determined by strain measurements and cooling time estimates compare favorably with predicted strain rates from the flow laws close to the intrusion (from the pluton to ~30 m away) (Figure 17) and indicate a geologically fast emplacement; however, at distances greater than 30 m from the contact the measured strain rates become much higher (up to 4 orders of magnitude faster) than the predicted strain rates. Measured strain rate values may be too high due to the difficulty of measuring strain of less than 0.1 or an over-estimation on cooling rates at greater distances from the pluton, and strain rates predicted from the flow laws may be too low due to the assumptions of constant stress and constant magma pressure.

Deformation mechanism maps (Figure 19), determined by manipulating the flow laws, provide a visual representation of the dislocation creep and diffusion creep fields, the boundary for which is grain size dependent, and the differential stress and temperature conditions necessary to initiate each. For the smallest grain sizes recorded over the traverse the stress and temperature constraints place the dolomite very close to the dislocation creep-diffusion creep boundary (Figure 19a). Calculated strain rates for this grain size agree with the predicted values which supports the possibility of mixed mechanism deformation. The deformation maps for larger grains sizes, however, are clearly indicative of dislocation creep (Figures 19b, 19c) given the constraints.

Additionally, studies have shown that steady state flow is achieved when approaching the dislocation creep-diffusion creep boundary and that dynamic recrystallization is responsible for a combination of grain size reduction and grain growth processes close to this boundary (De Bresser et al. 1998, De Bresser et al., 2001). This could suggest that evidence of original strain is wiped out via dynamic recrystallization and be responsible for an underestimate of strain within the metamorphic aureole.

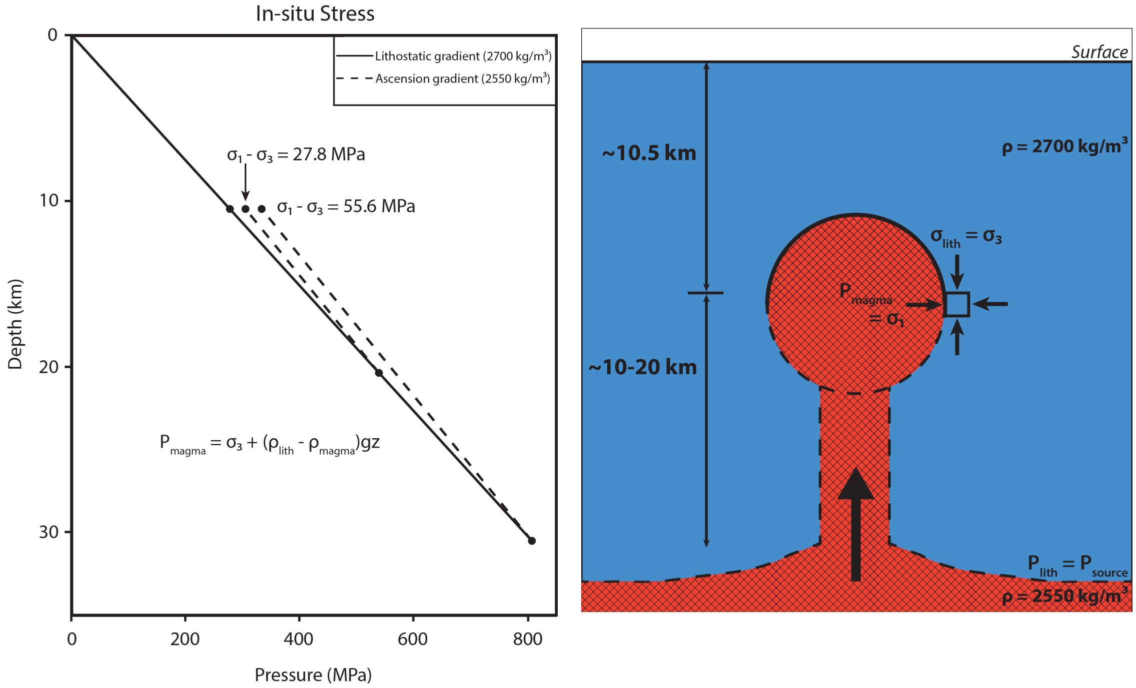

Figure 18. Estimation of in-situ differential stress. A pressure gradient of host rock (assuming average estimated density of 2.7 g/cm^3) and ascension of granitic melt (assuming granite melt density of 2.55 g/cm^3) from depths of 20.5 km and 30.5 km (10 and 20 km deeper than final emplacement depth, respectively) allow for estimations of differential stress at the time of emplacement. Using the provided equation the differential stress was calculated to be between 27.8 to 55.6 MPa. It is assumed that σ_3 is equal to lithostatic stress and σ_1 is equal to the magma pressure.

Figure 19. Deformation mechanism maps. Deformation mechanism maps for dolomite with grain sizes representative of the dolostones of the Kern Mountains. The bounding box in each figure represents the constraints of differential stress (27.8-55.6 MPa) and temperature (540°-640°C for d=35µm and d=70µm, 425°-575°C for d=150µm) determined for the Kern Mountain dolostones. (A) Deformation mechanism map assuming a grain size of 35 µm (observed ~17 m from the pluton). The calculated strain rate for dolomite ~17 m from the pluton is provided in the constraints box. The stress and temperature constraints suggest the possibility for dislocation creep, diffusion creep, or mixed mechanism deformation. (B) Deformation mechanism map for dolomite with a grain size of 70 µm (observed ~4 m from the pluton). The calculated strain rate for dolomite ~4 m from the pluton is provided in the constraints box. The stress and temperature constraints indicate dislocation creep. (C) Deformation mechanism map assuming a grain size of 150 µm (observed ~93 m from the pluton). The calculated strain rate for dolomite ~93 m from the pluton is provided in the constraints box. The stress and temperature constraints suggest dislocation creep.

A.

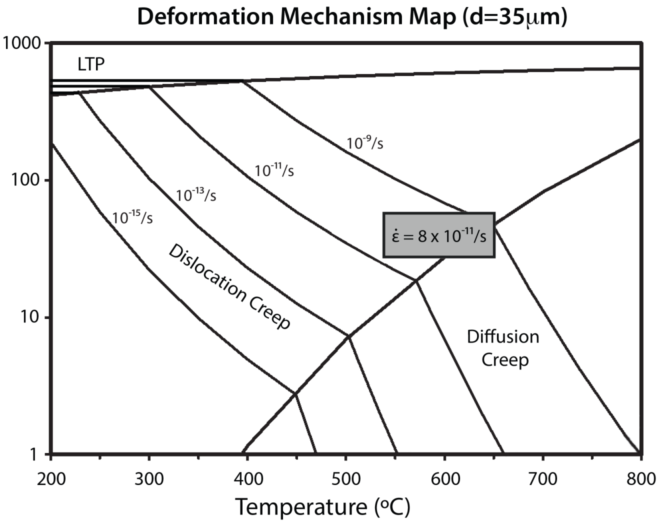
Deformation Mechanism Map (d=35μm)
LTP
10^{-9}/s
10^{-11}/s
10^{-13}/s
10^{-15}/s
$\dot{\varepsilon} = 8 \times 10^{-11}$/s
Dislocation Creep
Diffusion Creep
Differential stress (MPa)
1000
100
10
1
200
300
400
500
600
700
800
Temperature (°C)

B.

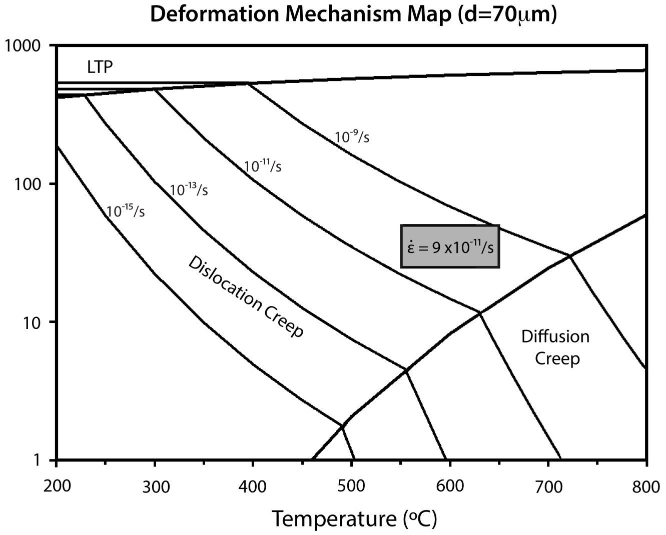
Deformation Mechanism Map (d=70μm)
LTP
10^{-9}/s
10^{-11}/s
10^{-13}/s
10^{-15}/s
$\dot{\varepsilon} = 9 \times 10^{-11}$/s
Dislocation Creep
Diffusion Creep
Differential stress (MPa)
1000
100
10
1
200
300
400
500
600
700
800
Temperature (°C)

C.

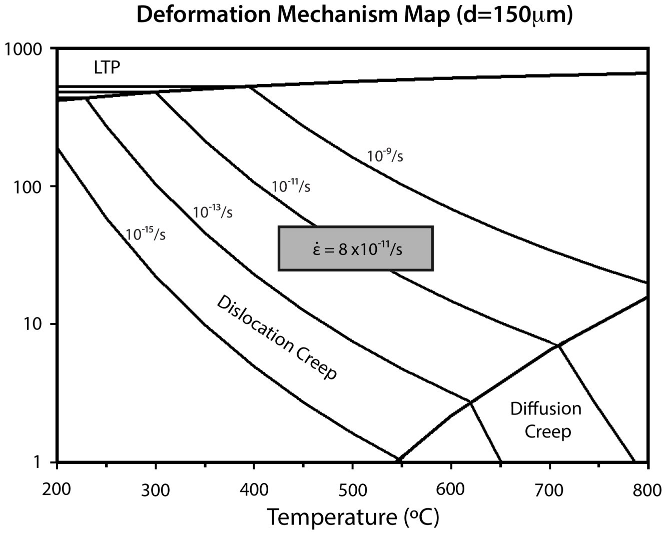
Deformation Mechanism Map (d=150μm)
LTP
10^{-9}/s
10^{-11}/s
10^{-13}/s
10^{-15}/s
$\dot{\varepsilon} = 8 \times 10^{-11}$/s
Dislocation Creep
Diffusion Creep
Differential stress (MPa)
1000
100
10
1
200
300
400
500
600
700
800
Temperature (°C)

5.3 Strain rate-temperature relationship

Strain rate calculated (predicted) from the experimentally defined flow laws range from 2×10^{-10} to 3×10^{-11} s^{-1} near the contact (up to 30 m away), which match with inferred strain rates close to the intrusion, and 2×10^{-15} to 2×10^{-16} s^{-1} far from the contact. Despite the shortcomings of my methods of estimating strains as a function of distance, thermal weakening of the dolostones is implied by large strains (and inferred strain rates) near the granite-dolostone contact while strains are smaller at greater distances from the contact. This is consistent qualitatively with dislocation and diffusion creep flow laws evaluated in experimental studies of Davis et al. (2008), Delle Piane et al. (2008), and Holyoke et al. (2013). The activation energies for dislocation creep are 145 kJ/mol (Holyoke et al., 2013), while activation energies for diffusion creep are larger, 280 kJ/mol (Davis et al., 2008) and 368 kJ/mol (Delle Piane et al., 2008). Lower values of activation energy are implied for the Kern Mountain dolostones, but this may only be due to difficulties in evaluating strains (and strain rates) from dolomite grain shapes. Nevertheless, strain rates near the granite-dolostone contact (Figure 17) are close to those predicted by flow laws.

5.4 Deformation mechanisms

Undulatory extinction, core and mantle structures, and recrystallization are associated with dislocation creep of dolomite (Davis et al., 2008; Wells et al., 2014) and can be observed in the Kern Mountain dolostones from the pluton contact to ~160 m away. In addition, the calculated strain rates for the dolostones, derived from measured strain and estimated cooling times, compare favorably with the total strain rates determined from the flow laws for dislocation creep close to the intrusion (up to ~30 m from the contact) (Figure 17). When I use the flow laws for dislocation and diffusion creep, I obtain diffusion creep rates that are comparable to dislocation creep rates near the granite-dolostone contact but find much lower contributions of diffusion creep further from the contact.

Deformation mechanism maps constructed for the measured grain sizes of dolostones surrounding the Tungstonia granite, estimates of stress and temperature, and reported flow laws for dislocation creep and diffusion creep, suggest that dislocation creep is predominant throughout the deformation aureole (Figure 19). Diffusion creep appears to be most important near the granite-dolostone contact, with ratios of dislocation creep to diffusion creep nearby one at the contact. Further from the contact, the calculated ratio of dislocation creep to diffusion creep increases dramatically (Figure 19).

Studies of natural and experimental deformation of dolomite have suggested that a LPO can be formed by dislocation creep, diffusion creep, or a mixed mechanism of the two (Davis et al., 2008; Delle Piane et al., 2008; Holyoke et al., 2013; Wells et al., 2014), so the development of a LPO near the granite-dolostone boundary may be associated with a number of deformation mechanisms (Davis et al., 2008; Delle Piane et al., 2008; Wells et al., 2014). However, the LPO observed in the Kern Mountain dolostones is consistent with LPO measured for experimentally sheared dolomites, deformation by diffusion creep (Delle Piane et al., 2008) with asymmetric c-axis patterns that are consistent with simple shear. Diffusion creep near the granite-dolostone contact may have been facilitated once strains by dislocation creep led to recrystallization and grain size refinement (Holyoke et al., 2014). Near the contact, strain rates may have been due to both dislocation and diffusion creep much as expected for steady-state creep accompanied by recrystallization and grain growth (de Bresser et al., 1988; Austin & Evans, 2007). Further from the granite-dolostone contact, coarse-grained dolomite appears to have deformed solely by dislocation creep with strains that were not sufficient to generate significant LPO (Figures 12 & 20).

The LPO of dolostones from this study are consistent with observations of experimental deformation of dolomite surrounding the Adamello pluton (Delle Piane et al., 2008). The relatively weak c-axes maxima, which are asymmetrical and antithetic to the direction of shear, weak a-axes girdle, and evidence for creep are in agreement with the granite-up/dolostone-down channel flow reported (Delle Piane et al., 2008). The orientation in which c-axes maxima align relative to shear sense is especially similar (within ~5°) between their findings and the LPO of this study (Delle Piane et al., 2008). If the LPO present in the Kern Mountain dolostones was stronger further from away from the granite-dolostone contact, evidence of channel flow may have been found; however, this is not observed.

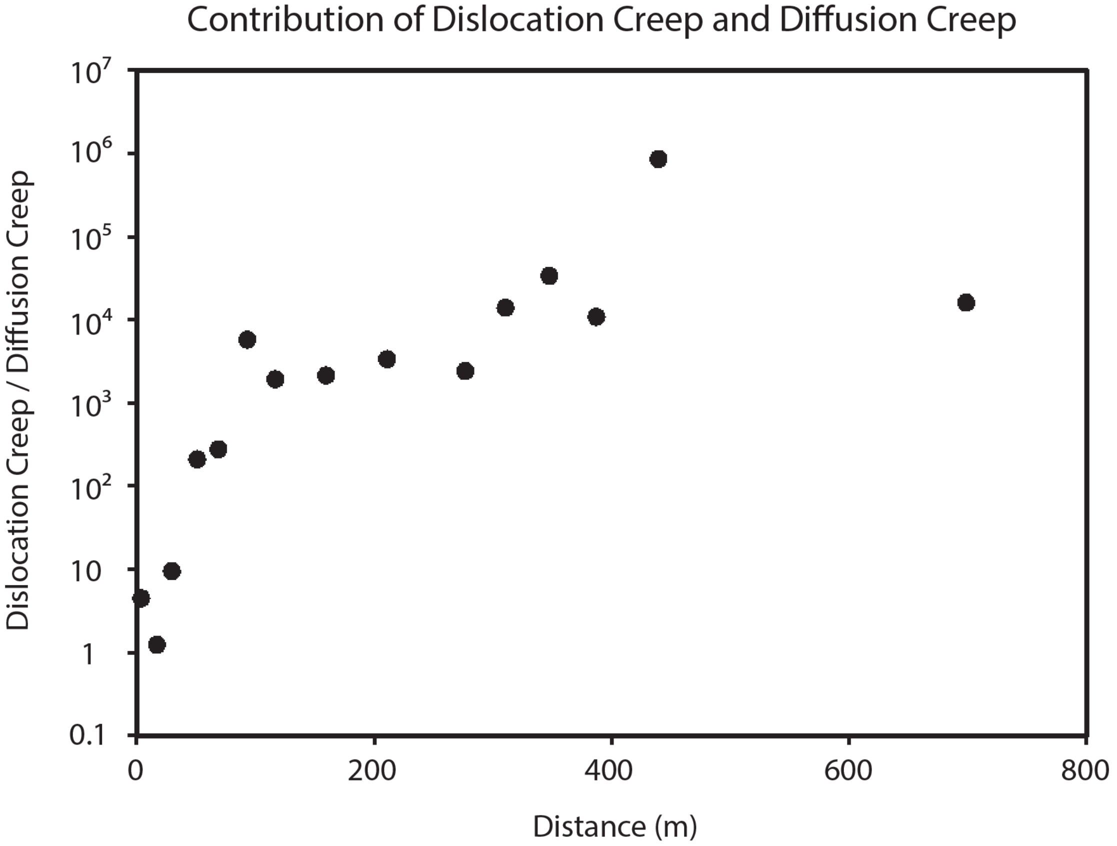

Figure 20. Relative contributions of dislocation creep and diffusion creep. Relative contributions expected from dislocation creep and diffusion creep as calculated from the flow laws plotted on a logarithmic scale with increasing distance from the intrusion. Ratios equal to 1 (at ~17 m) indicates an equal contribution predicted for both creep mechanisms and suggests mixed mechanism deformation. A ratio value of 10 indicates a 10-to-1 ratio of dislocation creep to diffusion creep, indicating dislocation is the dominant mechanism and diffusion creep is minor. Any ratio value greater than 100 suggests dislocation creep is dominant and minimal contributions from diffusion creep. Dolomite grains closest to the intrusion (up to ~30 m from the contact) are predicted to exhibit mixed mechanism deformation or dislocation creep dominance with minor diffusion creep. Dolomite grains farther than ~30 m from the intrusion are predicted to have negligible contributions from diffusion creep.

5.5 Comparison with previous studies

5.5.1 Natural dolomite deformation

Dolomites deformed at low temperatures and pressures generally show interval deformation and failure by fracture instead (Reeder & Wenk, 1979; Newman & Mitra, 1994; Billi, 2010). However, dolomites deformed in the high temperature vicinity of the Alpine Adamello pluton exhibit penetrative deformation (Delle Piane et al., 2008). One significant difference between their study and this one is that microstructures and calculated strain rates of dolostones surrounding the Tungstonia granite appear to be due to dislocation creep while diffusion creep is inferred in dolomites surrounding the Adamello pluton (Delle Piane et al., 2008). Closer comparisons between deformed dolomites of the two deformation aureoles cannot be made without additional information about grain sizes and temperatures of deformation of the Alpine dolomites. The asymmetry of dolomite LPOs near the contact of the Tungstonia granite and dolostones are antithetic to the sense of shear, as observed in large shear strain experiments of Delle Piane et al. (2008). However, this asymmetry is opposite of LPO asymmetry reported by Leiss & Barber (1998). Field observations and deformation microstructures observed across the traverse are consistent with the crystal plastic deformations observed in other studies of dolomites deformed at high temperatures (Newman & Mitra, 1994; Leiss & Barber, 1998; Wells et al., 2014).

5.5.2 Strain rates and temperature-dependence of experimental deformation

Strain rates inferred from grain shapes and constraints on time of emplacement near the granite-dolostone contact are comparable to those predicted by experimentally derived flow laws (Davis et al., 2008; Delle Piane et al., 2008; Holyoke et al., 2013) but appear to be large at larger distances from the pluton-country rock contact. Comparisons with deformation mechanism maps imply that dislocation creep was dominant over a wide range of conditions but that strain rates due to dislocation creep and diffusion creep were comparable near the granite-dolostone contact.

5.5.3 Emplacement models

Grain shapes of dolostones deformed in the vicinity of the Tungstonia granite, plotted on a Flinn diagram indicate that strains are very closely described as plane strain and flattening strain consistent with strains predicted at the lateral margins of a rising magma diapir by numerical models of Schmeling et al. (1988). LPOs developed near the granite-dolostone contact are consistent with shear with a granite up/dolostone down shear sense (Delle Piane et al., 2008). Combined, these results are consistent with diapir models of forceful emplacement (Figure 21) (Marsh, 1982; Schmeling et al., 1988; Paterson et al., 1989) though evidence for channel flow of country rocks is lacking. The temperature profile indicates a very narrow high temperature metamorphic aureole (~300 m), unlike some broader temperature gradients around other plutons (Nyman et al., 1995; Polyansky et al., 2010) and significant penetrative strains are restricted to the nearest ~400 m. The results of this study suggest that thermal softening is important to intrusion. In addition, the predominance of dislocation creep over diffusion creep indicates that strain may be further localized by nonlinear viscous response to emplacement forces (Paterson & Fowler, 1993; Weinberg & Podladchikov, 1994; Paterson & Miller, 1999; Polyansky et al., 2010).

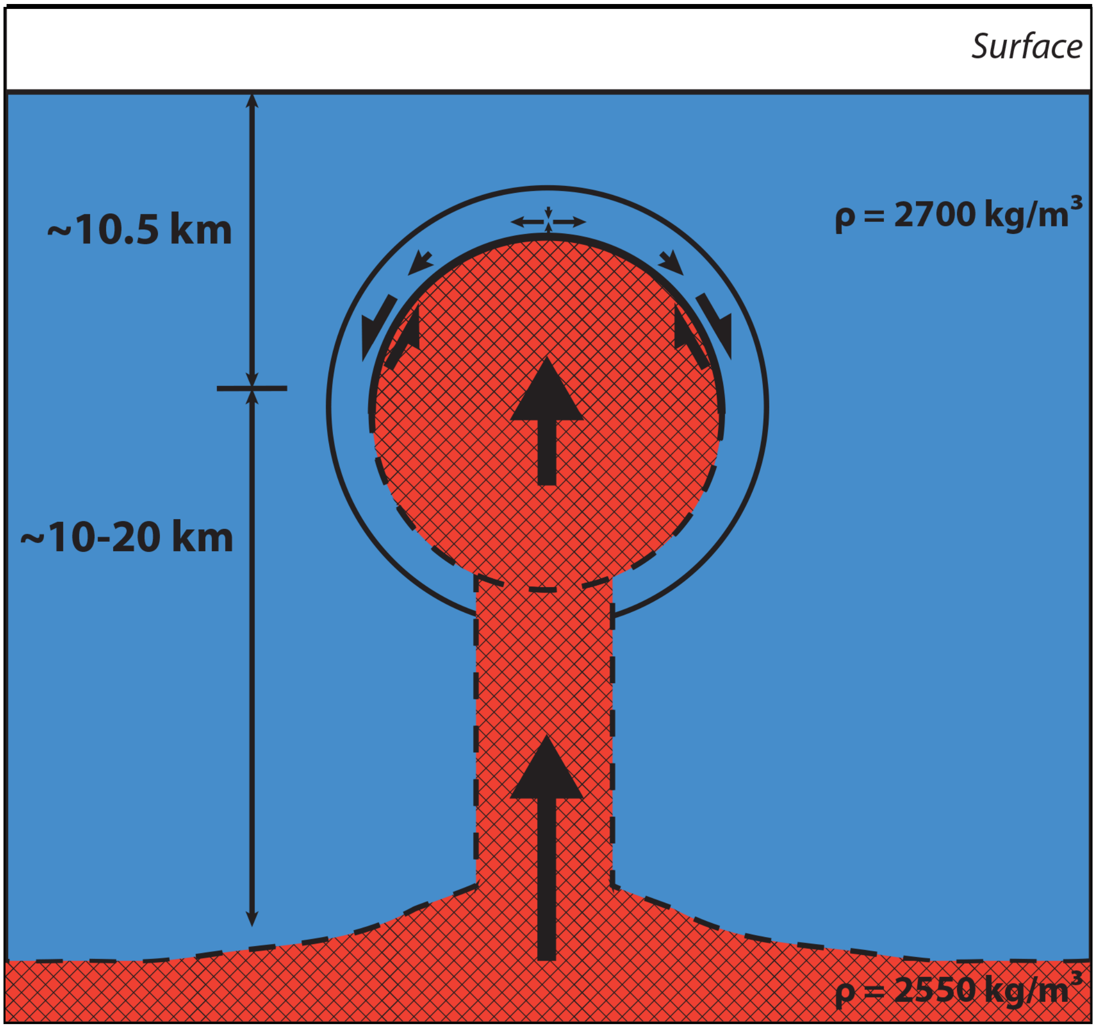

Figure 21. General emplacement model for the Tungstonia granite. Pure shear occurs at the top of the ascending body and transitions to simple shear out to the edges with channel flow inferred to displace the host rock. The lower part of the intrusion and original source depth are indicated with dashed lines, as the ascension process and source depth cannot be determined from this study.

VI. CONCLUSIONS

Microstructural, textural, and compositional study of dolostones surrounding the Tungstonia granite in the Kern Mountains, including measurements of grain size, grain shape, lattice-preferred orientations, mineral assemblages, and compositions, lead to a number of conclusions about the forceful emplacement of the Tungstonia granite into overlying dolostones:

- Penetrative strains localized within dolostones surrounding the Tungstonia granite are consistent with forceful, diapiric emplacement, with thermal softening in the high temperature metamorphic aureole.
- Dislocation creep is the dominant deformation mechanism in dolostones within ~400 m of the intrusion contact, while mechanism deformation (dislocation creep and diffusion creep) is possible from the pluton to ~30 m away. Thus, localized deformation in country rocks facilitating efficient diapiric flow is facilitated by non-linear flow laws of dislocation creep.
- Strain rates (of 9×10^{-11} s^{-1}) inferred from finite strains and emplacement times at estimated stresses, temperatures, and grain sizes are in agreement with strain rates predicted by experimentally derived flow laws for dislocation creep (and diffusion creep) of dolomite.

REFERENCES

Ahlborn, R. C., 1977. Mesozoic-Cenozoic structural development of the Kern Mountains, eastern Nevada-western Utah. Brigham Young University Research Studies, Geology Series 24, Part 2, 117-131.

Albertz, M., Johnson, S.E., 2006. Modeling dislocation creep as a near-field material transfer process during spherical pluton expansion: implications for strain rates and their preservation in pluton aureoles. Journal of Structural Geology 28, 253-267.

Anovitz, L.M., Essene, E.J., 1987. Phase equilibria in the system CaCO3-MgCO3-FeCO3. Journal of Petrology 28, 389-414.

Armstrong, R.L., 1968. Sevier orogenic belt in Nevada and Utah. Geological Society of America Bulletin 79, no. 4, 429-458.

Armstrong, R.L., 1972. Low-angle (denundation) faults, hinterland of the Sevier orogenic belt, eastern Nevada and western Utah. Geological Society of America Bulletin 83, 1729-1754.

Austin, N.J., Evans, B., 2007. Paleowattmeters: a scaling relation for dynamically recrystallized grain size. Geology 35, 343-346.

Barber, D.J., 1977. Defect microstructures in deformed and recovered dolomites. Tectonophysics 39, iss. 1-3, 193-213.

Barber, D.J., Heard, H.C., Paterson, M.S., Wenk, H.R., 1977. Stacking faults in dolomite. Tectonophysics 39, 193-213.

Barber, D.J., Heard, H.C., Wenk, H.R., 1981. Deformation of dolomite crystals from 20-800°C. Physics and Chemistry of Minerals 7, 271-286.

Barber, D.J., Wenk, H.R., Heard, H.C., 1994. The plastic deformation of polycrystalline dolomite: comparison of experimental results with theoretical predictions. Materials Science and Engineering 175, iss. 1-2, 83-104.

Barber, D.J., Wenk, H.C., 2001. Slip and dislocation behaviour in dolomite. European Journal of Mineralogy 13, no. 2, 221-243.

Barton, M. D., Trim, H. E., 1991. Late Cretaceous two-mica granites and lithophile-element mineralization in the Great Basin. In: Schafer, R. W., Wilkinson, W. H. (Eds.), Geology and Ore Deposits of the Great Basin, Geological Society of Nevada Symposium Proceedings, Geological Society of Nevada, 529-538.

Best, M., Armstrong, R., Graustein, W., Embree, G., Ahlborn, R., 1974. Mica granites of the Kern Mountains pluton, eastern White Pine County, Nevada, remobilized basement of the Cordilleran miogeosyncline. Geological Society of America Bulletin 85, no. 8, 1277-1286.

Best, M., 2003. Igneous and metamorphic petrology, 2nd ed. Berlin: Wiley-Blackwell Publishing, 729 p.

Billi, A., 2010. Microtectonics of low-P low-T carbonate fault rocks. Journal of Structural Geology 32, 1392-1402.

Brown, M., Solar, G.S., 1999. The mechanism of ascent and emplacement of granite magma during transpression: a syntectonic granite paradigm. Tectonophysics 312, 1-33.

Camilleri, P.A., 1996. Evidence for Late Cretaceous-Early Tertiary (?) extension in the Pequop Mountains, Nevada: implications for the nature of the Early Tertiary Unconformity. In: Taylor, W.J., Langrock, H. (Eds.), Cenozoic structure and stratigraphy of central Nevada: 1996 Field Conference Volume, Nevada Petroleum Society Inc., Reno, 19-28.

Clemens, J.D, Mawer, C.K. 1992. Granitic magma transport by fracture propagation. Tectonophysics 204**,** 339–360.

Clemens, J.D., 1998. Observations on the origins and ascent mechanisms of granitic magmas. Journal of the Geological Society, London 155, 843-851.

Clemens, J.D., Petford, N., Mawer, C.K., 1997. Ascent mechanisms of granitic magmas: causes and consequences. In: Holness, M. (Ed.), Deformation-enhanced Fluid Transport in the Earth's Crust and Mantle, Chapman & Hall, London, 144-171.

Clifford, P.M., 1972. Behavior of an Archean granitic batholith. Canadian Journal of Earth Sciences 9, 71-77.

Daly, R.A., 1903. The mechanics of igneous intrusion. American Journal of Science 16, 4th ser., 107-126.

Davis, N., Kronenberg, A., Newman, J., 2008. Plasticity and diffusion creep of dolomite. Tectonophysics 456, 127-146.

De Bresser, J.H.P., Peach, C.J., Reijs, J.P.J., Spiers, C.J., 1998. On dynamic recrystallization during solid-state flow: effects of stress and temperature. Geophysical Research Letters 25, no. 18, 3457-3460.

De Bresser, J.H.P., Ter Heege, J.H., Spiers, C.J., 2001. Grain size reduction by dynamic recrystallization: can it result in major rheological weakening?. International Journal of Earth Sciences 90, 28-45.

Delaney, P.T., Pollard, D.D., 1981. Deformation of host rocks and flow of magma during growth of minette dukes and breccia-bearing intrusions near Ship Rock, New Mexico. U.S. Geological Survey Professional Paper 1202, 1-61.

Delaney, P.T., Pollard, D.D., Ziony, J.I., McKee, E.H., 1986. Field relations between dikes and joints: emplacement processes and paleostress analysis. Journal of Geophysical Research 91, 4920-4938.

Delle Piane, C.D., Burlini, L., Kunze, K., Brack, P., Burg, J.P., 2008. Rheology of dolomite: large strain torsion experiments and natural examples. Journal of Structural Geology 30, 767-776.

Drewes, H., 1967. Geology of the Connors Pass quadrangle, Schell Creek Range, east-central Nevada. U.S. Geological Survey Professional Paper 557, 93 p.

Evans, B.W., 1965. Application of reaction-rate method to breakdown equilibria of muscovite and muscovite plus quartz. American Journal of Science 263, 647-667.

Gaudemer, Y., Tapponnier, P., 1987. Ductile and brittle deformations in the northern Snake Range, Nevada. Journal of Structural Geology 9, no. 2, 159-180.

Gerbi, C., Johnson, S.E., Paterson, S.R., 2004. Implications of rapid, dike-fed pluton growth for host-rock strain rates and emplacement mechanisms. Journal of Structural Geology 26, 583-594.

Gilbert, G.K., 1877. Report on the geology of the Henry Mountains. U.S. Geographical and Geological Survey of the Rocky Mountain Region, 160 p.

Goldsmith, J.R., Witters, J., Northruo, D.A., 1962. Studies in the system $CaCO_3$-$MgCO_3$-$FeCO_3$: a method for major-element spectrochemical analysis; 3. Composition of some ferroan dolomites. Journal of Geology 70, 659-687.

Grout, F.F., 1945. Scale models of structures related to batholiths. American Journal of Science 243, 260-284.

Gudmundsson, A., 1984. Formation of dykes, feeder-dykes, and the intrusion of dykes from magma chambers. Bulletin Volcanologique 47, iss. 3, 537-550.

Higgs, D.V., Handin, J., 1959. Experimental deformation of dolomite single crystals. Bulletin of the Geological Society America 70, 245-278.

Hintze, L.F., Kowallis, B.J., 2009. Geologic history of Utah: a field guide to Utah's rocks. Brigham Young University Geology Studies, Special Publications 9, 225 p.

Holder, M.T., 1979. An emplacement mechanism for post-tectonic granites and its implications for their geochemical features. In: Atherton, P.P., Tarney, J. (Eds.), Origin of granite batholiths; geochemical evidence: Orphington, England, Shiva, 148 p.

Holyoke, C.W., III, Kronenberg, A.K., Newman, J., 2013. Dislocation creep of polycrystalline dolomite. Tectonophysics 590, 72-82.

Holyoke, C.W., III, Kronenberg, A.K., Newman, J., 2014. Microstructural evolution during strain localization in dolomite. Journal of Structural Geology, 1-16.

Hose, R.K., Danes, Z.F., 1973. Development of Late Mesozoic to Early Cenozoic structures of the eastern Great Basin. In: DeJong, K.A., Scholten, R. (Eds.), Gravity and Tectonics, John Wiley and Sons, Inc., New York, 429-441.

Hose, R.K., Whitebread, D.H., 1981. Structural evolution of the central Snake Range, eastern Nevada during the Mid-to-Late Tertiary. Geological Society of America Abstract Programs 113, 62 p.

Hunt, C.B., Averitt, P., Miller, R.L., 1953. Geology and geography of the Henry Mountains region, Utah. U.S. Geological Survey Professional Paper 228, 234 p.

Hutton, D.H.W., 1988. Granite emplacement mechanisms and tectonic controls: inferences from deformation studies. Royal Society of Edinburgh Transactions 79, 245-255.

Kamb, W.B., 1959. Ice petrofabric observations from Blue Glacier, Washington, in relation to theory and experiment. Journal of Geophysical Research 64, no. 11, 1891-1909.

Kerrick, D.M., 1972. Experimental determination of muscovite + quartz stability with PH2O<PTotal. American Journal of Science 272, 946-958.

Lee, D.E., Kistler, R.W., Friedman, I., van Loenen, R.E., 1981. Two-mica granites of northeastern Nevada. Journal of Geophysical Research 86, no. B11, 10607-10616.

Lee, D.E., Christiansen, E.H., 1983. The granite problem as exposed in the southern Snake Range, Nevada. Contributions to Mineralogy and Petrology 83, 99-116.

Lee, D.E., Stacey, J.S.D., Fisher, L., 1986. Muscovite-phenocrystic two-mica granites of northeast Nevada are Late Cretaceous in age, in shorter contributions to isotope research. U.S. Geological Survey Bulletin 1622, 31-39.

Leiss, B., Barber, D.J., 1999. Mechanisms of dynamic recrystallization in naturally deformed dolomite inferred from EBSP analyses. Tectonophysics 303, 51-69.

Letargo, C.M.R., Lamb, W.M., Park, J.S., 1995. Comparison of calcite + dolomite thermometry and carbonate + silicate equilibria: constraints on the conditions of metamorphism of the Llano uplift, central Texas, U.S.A. American Mineralogist 80, 131-143.

Lister, J.R., Kerr, R.C., 1991. Fluid-mechanical models of crack propagation and their application to magma transport in dykes. Journal of Geophysical Research, no. B96, 10049–10077.

Marko, W., Yoshinobu, S., 2011. Using restored cross sections to evaluate magma emplacement, White Horse Mountains, eastern Nevada, U.S.A. Tectonophysics 500, 98-111.

Marsh, B., 1982. On the mechanics of igneous diapirism, stoping, and zone melting. American Journal of Science 282, 808-855.

Miller, E.L., Gans, P.B., 1989. Cretaceous crustal structure and metamorphism in the hinterland of the Sevier thrust belt, western U.S. Cordillera. Geology 17, 59-62.

Miller, E.L., Gans, P.B., Garing, J., 1983. The Snake Range décollement: an exhumed Mid-Tertiary ductile-brittle transition. Tectonics 2, no. 3, 239-263.

Miller, R.B., Paterson, S.R., 1999. In defense of magmatic diapirs. Journal of Structural Geology 21, 1161-1173.

Morgan, S.S., Law, R.D., Nyman, M.W., 1998. Laccolith-like emplacement model for the Papoose Flat pluton based on porphyroblast-matrix analysis. Geological Society of America Bulletin 110, 96-110.

Nelson, R.B., 1959. The stratigraphy and structure of the northernmost part of the northern Snake Range and the Kern Mountains in eastern Nevada and the southern Deep Creek Range in western Utah: PhD. Dissertation. University of Washington, 165 p.

Neumann, E.R., 1969. Experimental recrystallization of dolomite and comparison of preferred orientations of calcite and dolomite in deformed rocks. Journal of Geology 77, 426-438.

Newman, J., Mitra, G., 1994. Fluid-influenced deformation and recrystallization of dolomite at low temperatures along a natural fault zone, Mountain City window, Tennessee. Geological Society of America Bulletin 106, 1267-1280.

Nyman, M.W, Law, R.D., Morgan, S.S., 1995. Conditions of contact metamorphism, Papoose Flat pluton, eastern California, USA: implications for cooling and strain histories. Journal of Metamorphic Geology 13, 627-643.

Paterson, S.R., Vernon, R.H., Tobisch, O.T., 1989. A review of the criteria for the identification of magmatic and tectonic foliations in granitoids. Journal of Structural Geology 11, no. 3, 349-363.

Paterson, S.R., Fowler Jr., T.K., 1993. Extensional pluton-emplacement models: do they work for large plutonic complexes?. Geology 21, 781-784.

Paterson, S.R., Vernon, R.H., 1995. Bursting the bubble of ballooning plutons: a return to nested diapirs emplaced by multiple processes. Geological Society of America Bulletin 107, no. 11, 356-380.

Paterson, S.R., Miller, R.B., 1998. Mid-crustal magmatic sheets in the Cascades Mountains, Washington. Geological Society of America Bulletin 102, 1345-1363.

Paterson, S.R., Brudos, T., Fowler, K., Carlson, C., Bishop, K., Vernon, R.H., 2001. Papoose Flat pluton: forceful expansion or post-emplacement deformation?. Geology 19, 324-327.

Paterson, S.R., Okaya, D., Memeti, V., Economos, R., Miller, R.B., 2011. Magma addition and flux calculations of incrementally constructed magma chambers in continental margin arcs: combined field, geochronologic, and thermal modeling studies. Geosphere 7, no. 6, 1439-1468.

Petford, N., 1996. Dykes or diapirs?. Transactions of the Royal Society of Edinburgh: Earth Sciences 87, 105-114.

Petford, N., Kerr, R.C., Lister, J.R., 1993. Dike transport of granitic magmas. Geology 21, 843-845.

Pollard, D.D., 1973. Derivation and evaluation of a mechanical model for sheet intrusions. Tectonophysics 19, 233–269.

Pollard, D.D., Johnson, A.M., 1973. Mechanics of growth of some laccolithic intrusions in the Henry Mountains, Utah, Part 2. Tectonophysics 18, 311-354.

Pollard, D.D., 1976. On the form and stability of open hydraulic fractures in the Earth's crust. Geophysical Research Letters 3, no. 9, 513-516.

Pollard, D.D., Muller, O.H., 1976. The effect of gradients in regional stress and magma pressure on the form of sheet intrusions in cross section. Journal of Geophysical Research 81, no. 5, 975-984.

Polyansky, O.P., Korobeynikov, S.N., Babichev, A.V., Reverdatto, V.V., Sverdlova, V.G., 2009. Computer Modeling of Granite Magma Diapirism in the Earth's Crust. Doklady Earth Sciences 429, no. 8, 1380-1384.

Polyansky, O.P., Babichev, A.V., Korobeynikov, S.N., Reverdatto, V.V., 2010. Computer modeling of granite gneiss diapirism in the Earth's crust: controlling factors, duration, and temperature regime. Petrology 18, no. 4, 432-446.

Reeder, R.J., Wenk, H.R., 1979. Microstructures in low temperature dolomites. Geophysical Research Letters 6, no. 2, 77-80.

Reesor, J.E., 1958. Dewar Creek map area with special emphasis on the White Creek batholith, British Columbia. Geological Survey of Canada Memoir 292, 78 p.

Rosenberg, P.E., 1967. Subsolidus relations in the system $CaCO_3$-$MgCO_3$-$FeCO_3$ between 350 and 550°C. American Mineralogist 52, 787-797.

Saint-Blanquat, M. de, Law, R.D., Bouchez, J., Morgan, S.S., 2001. Internal structure and emplacement of the Papoose Flat pluton: an integrated structural, petrographic, and magnetic susceptibility. Geological Society of America Bulletin 113, no. 8, 976-995.

Sayeed, U.A., 1972. A note on the Kern Mountains plutonic complex, White Pine County, Nevada, and Juab County, Utah. Geological Society of America: Abstracts with Programs 4, no. 6, 407.

Sayeed, U.A., Treves, S.B., Nelson, R.B., 1973. Petrology of the Kern Mountains plutonic complex, White Pine County, Nevada, and Juab County, Utah. Geological Society of America: Abstracts with Programs 5, no. 6, 508.

Sayeed, U.A., Treves, S.B., Nelson, R.B., 1977. Geochemistry and hydrothermal alteration of the Kern Mountains plutonic complex, White Pine County, Nevada and Juab County, Utah. Geologische Rundschau 66, no. 1, 614-644.

Schmeling, H., Cruden, A., Marquart, G., 1988. Finite deformation in and around a fluid sphere moving through a viscous medium: implications for diapiric ascent. Tectonophysics 149, 17-34.

Shea, W.T., Kronenberg, A.K., Erksine, B., 1988. Diapiric emplacement of granitic magma: a natural example. Geological Society of America: Abstracts with Programs 20, A272.

Spera, F., 1980. Thermal evolution of plutons: a parameterized approach. Science 207, 299-301.

Sylvester, A.G., Oertel, G., Nelson, C.A., Christie, J.M., 1978. Papoose Flat pluton: a granitic blister in the Inyo Mountains, California. Geological Society of America Bulletin 89, 1205-1219.

Tikoff, B., de Saint Blanquat, M., Teyssier, C., 1999. Translation and the resolution of the pluton space problem. Journal of Structural Geology 21, 1109-1117.

Turcotte, G.L., Schubert, G., 2002. Geodynamics. Cambridge University Press, Cambridge, 456 p.

Weertman, J., 1971. Theory of water-filled crevasses in glaciers applied to vertical magma transport beneath oceanic ridges. Journal of Geophysical Research 76, 1171-1183.

Weinberg, R.F., Podladchikov, Y., 1994. Diapiric ascent of magmas through power law crust and mantle. Journal of Geophysical Research 99, no. B5, 9543-9559.

Weinberg, R.F., Podladchikov, Y., 1995. The rise of solid-state diapirs. Journal of Structural Geology 17, no. 8, 1183-1195.

Wells, R., Holyoke, C.W, III, Newman, J., Kronenberg, A.K., 2014. Lattice-preferred orientation development in fine-grained dolomite shear zones. Abstract T53C-2603, American Geophysical Union, Fall Meeting 2013, San Francisco, California, 9-13 December.

Wenk, H.-R., Barber, D.J., Reeder, R.J., 1983. Microstructures in carbonates. In: Carbonates: Mineralogy and Chemistry, Reeder, R.J. (Ed.), Reviews in Mineralogy 11, 301-361.

White, J.C., White, S.H., 1980. High-voltage transmission electron microscopy of naturally deformed polycrystalline dolomite. Tectonophysics 66, 35-54.

Zak, J., Paterson, S.R., 2006. Roof and walls of the Red Mountain Creek pluton, eastern Sierra Nevadas, California (USA): implications for process zones during pluton emplacement. Journal of Structural Geology 28, 575-587.

APPENDIX

Simple 1-D Thermal Model Work:

$$\theta = \frac{1 - \text{erf}\,(\eta)}{1 + \text{erf}\,(0.4)}$$

$$\theta = \frac{T - T_0}{T\eta - T_0} = \frac{1 - \text{erf}\,(\frac{x}{2\sqrt{\kappa t}})}{1.424}$$

For T=350, θ=0.22

$$\text{erf}(\eta) = 1 - 1.42\theta = 0.7$$

$$\eta \approx 0.75 = \frac{x}{2\sqrt{\kappa t}}$$

$$t = \frac{x^2}{4\kappa(0.75)^2}$$

$$t_{x=500} = 2200\, yrs.$$

Remaining EBSP plots

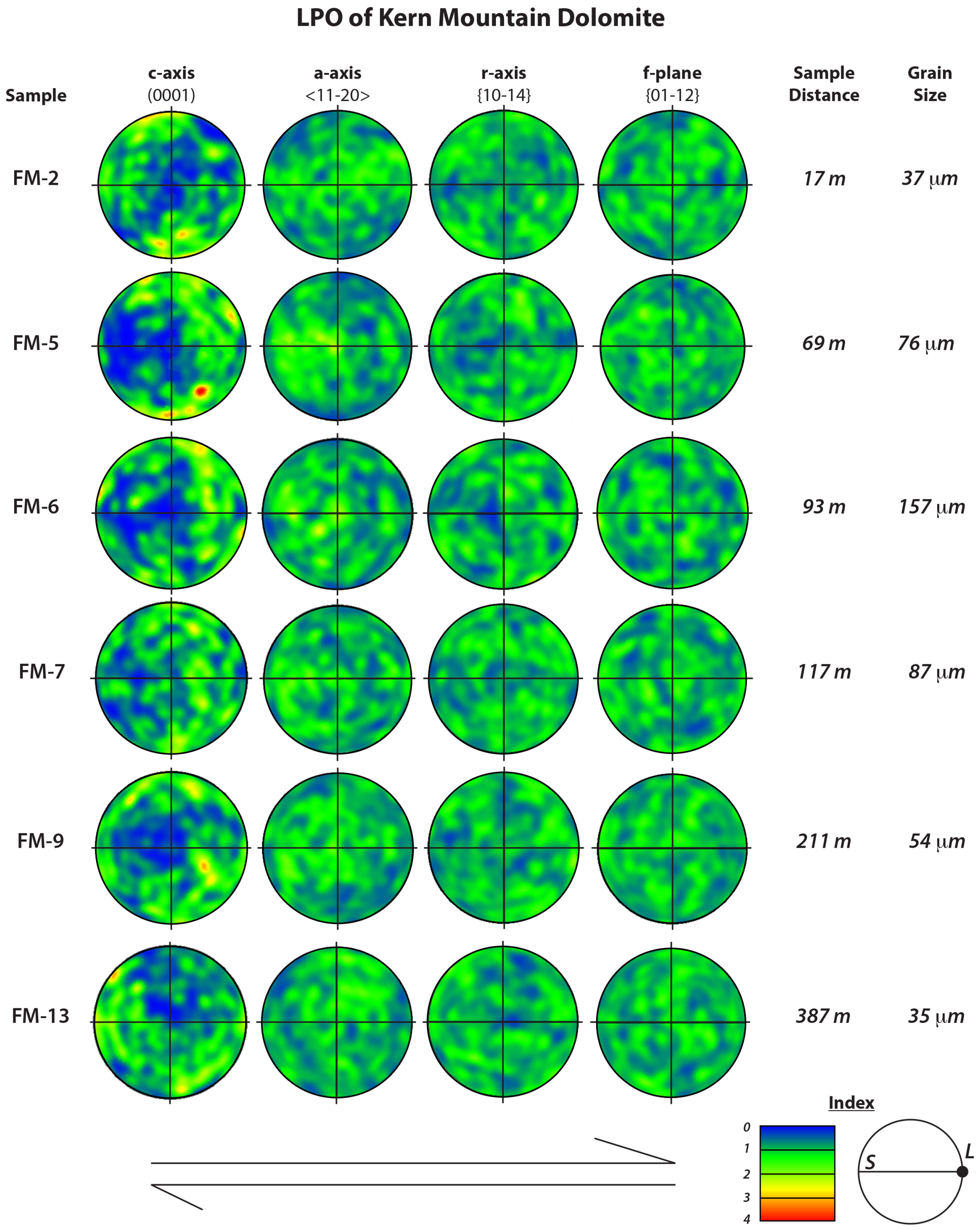

Example of aspect ration measurements, grain size determination, and strain inference.

FM-1	GRAIN	B MEASURED	ACTUAL B	Log(Actual B)	Avg. Log(B)	St. Dev.	C2 MEASURED	ACTUAL C2	Log(Actual C2)	Avg. Log(C2)	St. Dev.	ASPECT RATIO	Aspect Ratio (B/C)	CONVERSION	Average	Standard Deviation
A	1	2.2	60.1093	1.7789416	1.6499048	0.202817	1.2	32.78689	1.51570016	1.47700161	0.18117	0.55	1.833333333	27.3224044	**0.74167851**	0.343498
	2	0.7	19.1257	1.28161695			0.9	24.59016	1.39076142			1.29	0.777777778			
	3	0.8	21.8579	1.3396089			1	27.3224	1.43651891			1.25	0.8		Average (b/c)	St. De.
	4	1.4	38.2514	1.58264695		**10^x**	1.5	40.98361	1.61261017		**10^x**	1.07	0.933333333		1.641090915	0.739802
	5	3.95	107.923	2.03311601		44.65857	2.5	68.30601	1.83445892		29.9917	0.63	1.58			
	6	2.6	71.0383	1.85149226			0.9	24.59016	1.39076142			0.35	2.888888889			
	7	1.1	30.0546	1.4779116		**10^(x-s)**	1.15	31.42077	1.49721675		**10^(x-s)**	1.05	0.956521739		Avg A/Avg B	
	8	1.5	40.9836	1.61261017		27.9955	0.8	21.85792	1.3396089		19.7621	0.53	1.875		0.534047583	
	9	1	27.3224	1.43651891			0.8	21.85792	1.3396089	-	0.34108	0.80	1.25			
	10	1.025	28.0055	1.44724278		**10^(x+s)**	1.6	43.71585	1.6406389		**10^(x+s)**	1.56	0.640625			
	11	2.4	65.5738	1.81673016		71.23958	1.15	31.42077	1.49721675		45.5167	0.48	2.086956522		**For Grain Size Purposes**	
	12	2.8	76.5027	1.88367695			1.9	51.91257	1.71527252	+	0.51764	0.68	1.473684211		**Avg. A**	23.849802
	13	1.5	40.9836	1.61261017			0.45	12.29508	1.08973143			0.30	3.333333333		**Avg. B**	44.65857
	14	1.1	30.0546	1.4779116			0.825	22.54098	1.35297286			0.75	1.333333333		**Avg. C**	0
	15	1.8	49.1803	1.69179142			2.4	65.57377	1.81673016			1.33	0.75		**V=4/3*π*abc**	-
	16	1.35	36.8852	1.56685268			0.9	24.59016	1.39076142			0.67	1.5		**V=4/3*π*R^3**	
	17	1.2	32.7869	1.51570016			1	27.3224	1.43651891			0.83	1.2		**R=**	-
	18	2.25	61.4754	1.78870143			1	27.3224	1.43651891			0.44	2.25		**D=2*R**	-
	19	2.3	62.8415	1.79824675			1.2	32.78689	1.51570016			0.52	1.916666667			
	20	3.6	98.3607	1.99282142			1.55	42.34973	1.62685061			0.43	2.322580645			
	21	1.08	29.5082	1.46994267			1	27.3224	1.43651891			0.93	1.08			
	22	1.6	43.7158	1.6406389			0.5	13.6612	1.13548892			0.31	3.2			
	23	1.125	30.7377	1.48767144			0.7	19.12568	1.28161695			0.62	1.607142857		E3	#DIV/0!
	24	2.8	76.5027	1.88367695			1.5	40.98361	1.61261017			0.54	1.866666667		E2	#DIV/0!
	25	2.2	60.1093	1.7789416			1.4	38.25137	1.58264695			0.64	1.571428571		E1	#DIV/0!

FM-1New	GRAIN	A MEASURED	ACTUAL A	Log(Actual A)	Avg. Log(A)	St. Dev.	C1 MEASURED	ACTUAL C1	Log(Actual C1)	Avg. Log(C1)	St. Dev.	ASPECT RATIO	Aspect Ratio (a/b)	CONVERSION	AVERAGE ASPECT RATIO	Average	Standard Deviation	Log(a/c)	Avg. Log(a/c)	St. Dev.
A	1	1.15	21.698113	1.336421971	1.377485	0.29871	1.15	21.6981132	1.336421971	1.18377391	0.284007	1		18.8679245	**1.665984722**	1.66598	0.6607989	0	0.19371086	0.1535
	2	0.3	5.6603774	0.752845385			0.25	4.71698113	0.673664139			1.2						0.07918		
	3	1.4	26.415094	1.421852166			0.6	11.3207547	1.053875381			2.3333333						0.36798		
	4	1.15	21.698113	1.336421971		**10^x**	0.75	14.1509434	1.150785394		**10^x**	1.5333333						0.18564		
	5	1.6	30.188679	1.479844113		23.8498	1.4	26.4150943	1.421852166		15.26771	1.1428571						0.05799		**10^x**
	6	2.1	39.622642	1.597943425			1.4	26.4150943	1.421852166			1.5						0.17609		1.56211
	7	1.03	19.433962	1.288561355		**10^(x-s)**	1	18.8679245	1.27572413		**10^(x-s)**	1.03						0.01284		
	8	2.63	49.622642	1.695679879		11.9887	2.1	39.6226415	1.597943425		7.939012	1.252381						0.09774		**10^(x-s)**
	9	2.5	47.169811	1.673664139			1.25	23.5849057	1.372634143			2						0.30103		1.09702
	10	3.15	59.433962	1.774034684		**10^(x+s)**	1.8	33.9622642	1.530996636		**10^(x+s)**	1.75						0.24304		
	11	1.45	27.358491	1.437092133		47.4456	1.2	22.6415094	1.354905376		29.36171	1.2083333						0.08219		**10^(x+s)**
	12	1.1	20.754717	1.317116816			0.92	17.3584906	1.239511958			1.1956522						0.0776		2.22436
	13	2.16	40.754717	1.610177882			2.02	38.1132075	1.5810755			1.0693069						0.0291		
	14	0.65	12.264151	1.088637487			0.4	7.54716981	0.877784122			1.625						0.21085		
	15	0.3	5.6603774	0.752845385			0.25	4.71698113	0.673664139			1.2						0.07918		
	16	0.9	16.981132	1.22996664			0.83	15.6603774	1.194802223			1.0843373						0.03516		
	17	1.5	28.301887	1.451815389			0.73	13.7735849	1.139046991			2.0547945						0.31277		
	18	1.9	35.849057	1.554477731			1.35	25.4716981	1.406057899			1.4074074						0.14842		
	19	1.8	33.962264	1.530996636			0.6	11.3207547	1.053875381			3						0.47712		
	20	1.05	19.811321	1.296913429			0.3	5.66037736	0.752845385			3.5						0.54407		
	21	0.85	16.037736	1.205143056			0.45	8.49056604	0.928936644			1.8888889						0.27621		
	22	3.6	67.924528	1.832026631			1.4	26.4150943	1.421852166			2.5714286						0.41017		
	23	0.7	13.207547	1.12082217			0.52	9.81132075	0.991727474			1.3461538						0.12909		
	24	0.4	7.5471698	0.877784122			0.3	5.66037736	0.752845385			1.3333333						0.12494		
	25	3.15	59.433962	1.774034684			1.3	24.5283019	1.389667483			2.4230769						0.38437		

Example of microprobe data

```
Analysis no.    7 within  carbdolo

 Elt.        Conc.    1sigma   Norm Conc.  Norm Conc.
Compound        Concen.
             (wt%)     (wt%)    (wt%)      (at%)
(wt%)
   Na        0.0094   0.003216     0.0093     0.0075
Na2O            0.013
   Si        0.0023   0.003863     0.0023     0.0015
SiO2            0.005
   Mg       13.1713   0.065711    13.0562     9.9139
MgO            21.842
   Al        0.0000   0.000000     0.0000     0.0000
Al2O3
   Ca       22.0489   0.083069    21.8563    10.0640
CaO            30.851
   Sr        0.0111   0.012401     0.0110     0.0023
SrO             0.013
   S         0.0019   0.002527     0.0019     0.0011
SO3             0.005
   Fe        0.0216   0.006501     0.0214     0.0071
FeO             0.028
   Mn        0.0082   0.005549     0.0081     0.0027
MnO             0.011
   C        13.1310    13.0163    20.0000      CO2
48.115
   O        52.4757    52.0172    60.0000  oxide-like spec.

  total :  100.8814             100.0000   100.0000
100.881

     be careful, strong correction for Al ( 0.00)

     carbonate        cations on  6. <o> basis

                                    Wt.%    Cations
  S(CO3)3       0.0124        S    0.0019    0.0001
  Si(CO3)2      0.0124        Si   0.0023    0.0002
  Al2(CO3)3     0.0000        Al   0.0000    0.0000
  Mg(CO3)      45.7356        Mg  13.1713    0.9914
  Ca(CO3)      55.1063        Ca  22.0489    1.0064
  Mn(CO3)       0.0172        Mn   0.0082    0.0003
  Fe(CO3)       0.0447        Fe   0.0216    0.0007
  Sr(CO3)       0.0187        Sr   0.0111    0.0002
  Na2(CO3)      0.0217        Na   0.0094    0.0007
  total       100.9690                       2.0000

  Ratio (Fe+Mn)/(Fe+Mn+Mg) =   0.10

  point n :     8     x=    3829.0  y=   27628.0  z=    13.
carbdolo
                        FM_9_qa_8
```

```
 Elt.  Line Xtal  Spec.    Std.    Posi.
Beam    Acceleration

(nA)     voltage(kV)

49.8      15.0
  Na    Ka  TAP    Sp1  5albite    46375
  Si    Ka  TAP    Sp1  5albite    27737
  Mg    Ka  TAP    Sp2  3dolomite  38495
  Al    Ka  TAP    Sp2  5albite    32464
  Ca    Ka  PET    Sp3  3dolomite  38383
  Sr    La  PET    Sp3  3strontia  78456
  S     Ka  PET    Sp3  5BaSO4     61385
  Fe    Ka  LIF    Sp4  3siderite  48078
  Mn    Ka  LIF    Sp4  5spessart  52204

 Elt.  Peak   Prec.  Bkgd     P/B   Ix/  Sig/k   Detection
Beam    Acceleration
       (Cps)   (%)   (Cps)          Istd   (%)    limit (%)
(nA)     voltage(kV)

49.8      15.0
  Na      14.9  3.3    12.9     1.16 0.0009   3.4     0.0048
  Si      83.7  2.4    55.4     1.51 0.0014   2.4     0.0042
  Mg    5205.1  0.4    20.7   251.44 0.9801   0.5     0.0198
  Al      42.2  3.4    31.6     1.34 0.0017   3.5     0.0040
  Ca    8183.9  0.3    54.9   149.05 1.0239   0.4     0.0341
  Sr       2.0  9.2     2.1     0.92 0.0000   9.2     0.0000
  S        7.4  4.7     6.0     1.23 0.0005   4.8     0.0040
  Fe      12.5  3.4    10.4     1.19 0.0004   3.5     0.0095
  Mn       8.3  4.2     8.8     0.94 0.0000   4.2     0.0000

 Elt.      k-ratio    Correc.
  Na        0.0000     2.1815
  Si        0.0003     1.3379
  Mg        0.0801     1.6187
  Al        0.0001     1.5928
  Ca        0.2008     1.1056
  Sr        0.0000   NaN
  S         0.0001     1.1547
  Fe        0.0002     1.2565
  Mn        0.0000   NaN

  iteration :  2
```